

TOOLS AND RESOURCES

Insights into animal septins using recombinant human septin octamers with distinct SEPT9 isoforms

Francois Iv¹, Carla Silva Martins¹, Gerard Castro-Linares², Cyntia Taveneau^{3,4}, Pascale Barbier⁵, Pascal Verdier-Pinard⁶, Luc Camoin⁷, Stéphane Audebert⁷, Feng-Ching Tsai^{8,*}, Laurie Ramond¹, Alex Llewellyn¹, Mayssa Belhabib¹, Koyomi Nakazawa³, Aurélie Di Cicco³, Renaud Vincentelli⁹, Jerome Wenger¹, Stéphanie Cabantous¹⁰, Gijse H. Koenderink^{2,8,‡}, Aurélie Bertin^{3,‡} and Manos Mavragis^{1,‡}

ABSTRACT

Septin GTP-binding proteins contribute essential biological functions that range from the establishment of cell polarity to animal tissue morphogenesis. Human septins in cells form hetero-octameric septin complexes containing the ubiquitously expressed SEPT9 subunit (also known as SEPTIN9). Despite the established role of SEPT9 in mammalian development and human pathophysiology, biochemical and biophysical studies have relied on monomeric SEPT9, thus not recapitulating its native assembly into hetero-octameric complexes. We established a protocol that enabled, for the first time, the isolation of recombinant human septin octamers containing distinct SEPT9 isoforms. A combination of biochemical and biophysical assays confirmed the octameric nature of the isolated complexes in solution. Reconstitution studies showed that octamers with either a long or a short SEPT9 isoform form filament assemblies, and can directly bind and cross-link actin filaments, raising the possibility that septin-decorated actin structures in cells reflect direct actin–septin interactions. Recombinant SEPT9-containing octamers will make it possible to design cell-free assays to dissect the complex interactions of septins with cell membranes and the actin and microtubule cytoskeleton.

KEY WORDS: Human septins, SEPT9 isoforms, Cytoskeleton, Electron microscopy, Analytical ultracentrifugation, Mass spectrometry, *In vitro* reconstitution, Protein biochemistry

INTRODUCTION

Septins constitute a family of GTP-binding proteins that is conserved from algae and protists to mammals (Cao et al., 2007; Momany et al., 2008; Nishihama et al., 2011; Pan et al., 2007). Septins are involved in a wide range of biological processes, from the establishment of cell polarity and cell division to cell–cell adhesion, cell motility, animal tissue morphogenesis and infection (Fung et al., 2014; Marquardt et al., 2019; Mostowy and Cossart, 2012; Weirich et al., 2008). In human pathophysiology, a role of septins has been established in neuropathies, infertility and tumorigenesis (Dolat et al., 2014a; Montagna et al., 2015). Despite their essential roles, how human septins organize and function in cells remains much more poorly understood than for budding yeast, in which septins were first discovered (Hartwell, 1971; Hartwell et al., 1970). Mammalian septins are thought to associate with cell membranes (Akil et al., 2016; Bridges et al., 2016; Damalio et al., 2013; Dolat and Spiliotis, 2016; Omrane et al., 2019; Tanaka-Takiguchi et al., 2009; Zhang et al., 1999), like their yeast counterparts (Bertin et al., 2010; Bridges et al., 2016; Bridges et al., 2014; Casamayor and Snyder, 2003). Mammalian septins localize extensively to actin and microtubules in cells, for example to the ingressing cytokinetic ring in dividing cells (Estey et al., 2010; Joo et al., 2007; Kim et al., 2011; Kinoshita et al., 1997; Surka et al., 2002), stress fibers in interphase cells (Calvo et al., 2015; Connolly et al., 2011; Dolat et al., 2014b; Joo et al., 2007; Kim et al., 2011; Kinoshita et al., 2002; Kinoshita et al., 1997; Liu et al., 2014; Surka et al., 2002; Verdier-Pinard et al., 2017; Xie et al., 1999; Zhang et al., 1999), and to interphase, mitotic spindle and intercellular bridge microtubules (Bowen et al., 2011; Nagata et al., 2004; Nagata et al., 2003; Spiliotis et al., 2008; Spiliotis et al., 2005; Surka et al., 2002; Verdier-Pinard et al., 2017). Mammalian septin association with membranes as well as with the actin and microtubule cytoskeleton has made it difficult to dissect how they function, and at the same time raises the intriguing possibility that septins mediate cytoskeleton–membrane cross-talk.

Studies of native and recombinant septins isolated from budding yeast (Bertin et al., 2008; Farkasovsky et al., 2005; Frazier et al., 1998; Garcia et al., 2011; Versele and Thorner, 2004), *Drosophila* (Field et al., 1996; Huijbregts et al., 2009; Mavragis et al., 2014), *C. elegans* (John et al., 2007), and mammalian cell lines and tissues (Hsu et al., 1998; Kim et al., 2011; Kinoshita et al., 2002; Sellin et al., 2011; Sirajuddin et al., 2007) have established that septins form heteromeric complexes, with each septin present in two copies, forming a palindrome. Phylogenetic analysis has classified human

¹Institut Fresnel, CNRS UMR7249, Aix Marseille Univ, Centrale Marseille, 13013 Marseille, France. ²Department of Bionanoscience, Kavli Institute of Nanoscience Delft, Delft University of Technology, 2629 HZ Delft, The Netherlands. ³Institut Curie, Université PSL, Sorbonne Université, CNRS UMR 168, Laboratoire Physico Chimie Curie, 75005 Paris, France. ⁴ARC Centre of Excellence in Advanced Molecular Imaging, Monash University, Australia; Biomedicine Discovery Institute, Department of Biochemistry and Molecular Biology, Monash University, 3800 Clayton, Australia. ⁵Aix-Marseille Univ, CNRS, UMR 7051, Institut de Neurophysiopathologie (INP), 13005 Marseille, France. ⁶Centre de Recherche en Cancérologie de Marseille (CRCM), INSERM, Institut Paoli-Calmettes, Aix Marseille Univ, CNRS, 13009 Marseille, France. ⁷Aix-Marseille Univ, INSERM, CNRS, Institut Paoli-Calmettes, CRCM, Marseille Protéomique, Marseille, France. ⁸Department of Living Matter, AMOLF, 1098 XG Amsterdam, The Netherlands. ⁹Architecture et Fonction des Macromolécules Biologiques (AFMB), CNRS UMR7257, Aix Marseille Univ, 13009 Marseille, France. ¹⁰Centre de Recherche en Cancérologie de Toulouse (CRCT), Inserm, Université Paul Sabatier-Toulouse III, CNRS, 31037 Toulouse, France.

*Present address: Institut Curie, Université PSL, Sorbonne Université, CNRS UMR 168, Laboratoire Physico Chimie Curie, 75005 Paris, France.

‡Authors for correspondence (manos.mavragis@univ-amu.fr, aurelie.bertin@curie.fr, G.H.Koenderink@tudelft.nl)

DOI: 10.1242/jcs.258484; F.I., 0000-0003-2630-9586; C.S.M., 0000-0002-5760-859X; C.T., 0000-0002-3395-4957; P.B., 0000-0002-0622-182X; P.V.-P., 0000-0002-6149-6578; L.C., 0000-0002-1230-4787; S.A., 0000-0002-9409-2588; F.-C.T., 0000-0002-6869-5254; L.R., 0000-0002-2555-6174; A.L., 0000-0002-9164-2409; M.B., 0000-0002-6603-7784; S.C., 0000-0002-8406-9421; G.H.K., 0000-0002-7823-8807; A.B., 0000-0002-3400-6887; M.M., 0000-0002-7980-1841

septins in four homology groups, namely the SEPT2 group (SEPT1, 2, 4 and 5), the SEPT6 group (SEPT6, 8, 10, 11 and 14), the SEPT7 group (SEPT7), and the SEPT3 group (SEPT3, 9 and 12) (Kinoshita, 2003; alternative symbols for septins are SEPTIN1–12, SEPTIN14; see Materials and Methods for nomenclature). Native human septins isolated from cells exist in the form of stable hexamers and octamers (Kim et al., 2011; Sellin et al., 2011, 2014). Hexamers are composed of septins from the SEPT2, SEPT6 and SEPT7 groups, while octamers contain additional septins from the SEPT3 group (Fig. 1A).

A well-documented feature of septins is that purified septin heteromeric complexes self-assemble into filaments (Valadares et al., 2017). Whether all native septin pools are filamentous, and how septin function is linked to the relative distributions of hexamers and octamers and their polymerization capacity within cells are not known. The most convincing evidence that septins form filaments *in vivo*, and that septin function depends on their ability to assemble into filaments, comes from budding yeast (Bertin et al., 2012; Byers and Goetsch, 1976; McMurray et al., 2011; Ong et al., 2014; Rodal et al., 2005).

A powerful tool for studying septin assembly and function has been the use of recombinant septin complexes. Earlier studies using recombinant mammalian septin complexes have combined septins from two or more species, most likely for pragmatic reasons. Mouse SEPT2 was combined with human SEPT6 and SEPT7 (Kinoshita et al., 2002; Mavrikakis et al., 2014; Sirajuddin et al., 2007), or with human SEPT6, SEPT7 and SEPT3 (DeRose et al., 2020), and mouse SEPT2 was also combined with human SEPT6 and rat SEPT7 (Bai et al., 2013). There are currently no studies showing whether these specific species-related differences affect septin function. Still, taking into account that these differences lie in exposed residues in the very N- or/and C-terminal extensions (Fig. 1A,B), or within exposed loops in the GTP-binding domain, and given how poorly we understand the factors that impact animal septin assembly and function, there is a clear need to produce septin complexes with full-length septins from one species, notably human septin octamers containing SEPT2, SEPT6, SEPT7 and SEPT9.

SEPT9 is the only septin from the SEPT3 group whose expression is ubiquitous across human tissues, with SEPT3 and SEPT12 being neuron- and testis-specific, respectively (Cao et al., 2007; Connolly et al., 2011; Hall et al., 2005). *Sept9* gene knockout in mice is embryonic lethal (Fuchtbauer et al., 2011), and a large body of literature has implicated SEPT9 in diverse human cancers (Dolat et al., 2014a; Montagna et al., 2015). There are five SEPT9 isoforms (SEPT9_i) differing in the length and composition of the N-terminal extension preceding the GTP-binding domain (Connolly et al., 2014; McIlhatton et al., 2001) (Fig. 1B). Distinct SEPT9 isoforms can have different functions, as reported for cytokinesis and cancer cell migration (Estey et al., 2010; Verdier-Pinard et al., 2017). Despite its importance in mammalian development and human pathophysiology, biochemical and biophysical studies of SEPT9 have been limited to the use of monomeric SEPT9 and fragments thereof (Bai et al., 2013; Dolat et al., 2014b; Nakos et al., 2019; Smith et al., 2015), thus not recapitulating its native assembly into hetero-octameric complexes (Sellin et al., 2011, 2014). Multiple studies have documented promiscuity in septin–septin interactions in the absence of their physiologically relevant binding partners, affecting the availability of specific structural elements for interactions with other septins or interacting proteins (Castro et al., 2020; Valadares et al., 2017). The need to study septins in the context of their native heteromeric complexes is highlighted by the increasing number of structural

studies of the factors governing the molecular specificity that determines the correct pairing of septins during complex assembly (Kumagai et al., 2019; Rosa et al., 2020; Sala et al., 2016).

The N-terminal extension in the long SEPT9 isoforms (SEPT9_i1, SEPT9_i2 and SEPT9_i3) is of considerable size (~27 kDa; i.e. three-quarters of the size of the GTP-binding domain) making these isoforms the longest, in terms of the number of residues, of all human septins. Given that the long SEPT9 isoforms differ only in the composition of their N-terminal 25, 18 and 7 residues, respectively (Fig. 1B and Fig. S1B for SEPT9_i1 and SEPT9_i3), it is intriguing that they all associate with actin stress fibers in cells, whereas only SEPT9_i1 associates with microtubules (Nagata et al., 2004; Nagata et al., 2003; Surka et al., 2002). Different cell types express different sets of SEPT9 isoforms, with some cell types expressing specific long SEPT9 isoforms, and others lacking long SEPT9 isoforms altogether (Burrows et al., 2003; Sellin et al., 2014; Verdier-Pinard et al., 2017). Hereditary neuralgic amyotrophy (HNA), a rare neuropathy, has been mapped to missense mutations and duplications in the large N-terminal extension shared by the long SEPT9 isoforms (Collie et al., 2010; Hannibal et al., 2009; Kuhlenbaumer et al., 2005; Landsverk et al., 2009). Understanding SEPT9 function thus necessitates the isolation of recombinant septin octamers bearing distinct SEPT9 isoforms.

To enable studies of SEPT9 function in the context of its physiological assembly into hetero-octamers, we established a protocol that enabled, for the first time, the isolation of recombinant human septin octamers containing distinct SEPT9 isoforms (Fig. 1B). A combination of biochemical and biophysical assays confirmed the octameric nature of the isolated octamers in solution, and also provided evidence for SEPT2 occupying the end positions in the octamer. Fluorescence and electron microscopy showed that recombinant octamers containing either a long or a short SEPT9 isoform form higher-order filament assemblies. As a first step towards the reconstitution of recombinant SEPT9-containing octamers with known physiological interactors, we examined their interactions with actin filaments. Reconstitution studies showed that octamers with either a long or a short SEPT9 isoform directly bind and cross-link actin filaments, raising the possibility that septin-decorated actin bundles in cells reflect direct actin–septin interactions. Biochemical and biophysical reconstitution studies of recombinant octamers containing distinct SEPT9 isoforms with physiological septin interactors, such as membranes and microtubules, promise to provide a powerful complementary approach to cell and animal model studies of septin organization and function.

RESULTS

A two-tag purification scheme yields stoichiometric recombinant human septin octamers containing distinct SEPT9 isoforms

To isolate octamers containing either a long SEPT9 isoform, in particular SEPT9_i1 and SEPT9_i3, or octamers containing a short SEPT9 isoform, SEPT9_i5 (Fig. 1B), we combined the pET multi-cloning and expression (pET-MCN) series as a septin co-expression system (Diebold et al., 2011) with a two-tag purification scheme. We used two bicistronic vectors – one vector co-expressing SEPT2 and SEPT6, and the other one SEPT7 and SEPT9_i (Fig. S1A). To minimally perturb septin complex assembly, and interactions with other proteins or membranes, we chose small (1 kDa) tags, a hexahistidine (His₆) tag and the eight-amino-acid Strep-tag II (Fig. S1B). To isolate octamers, we tagged the N-terminus of the end subunit, SEPT2, with a tobacco etch virus (TEV) protease-cleavable

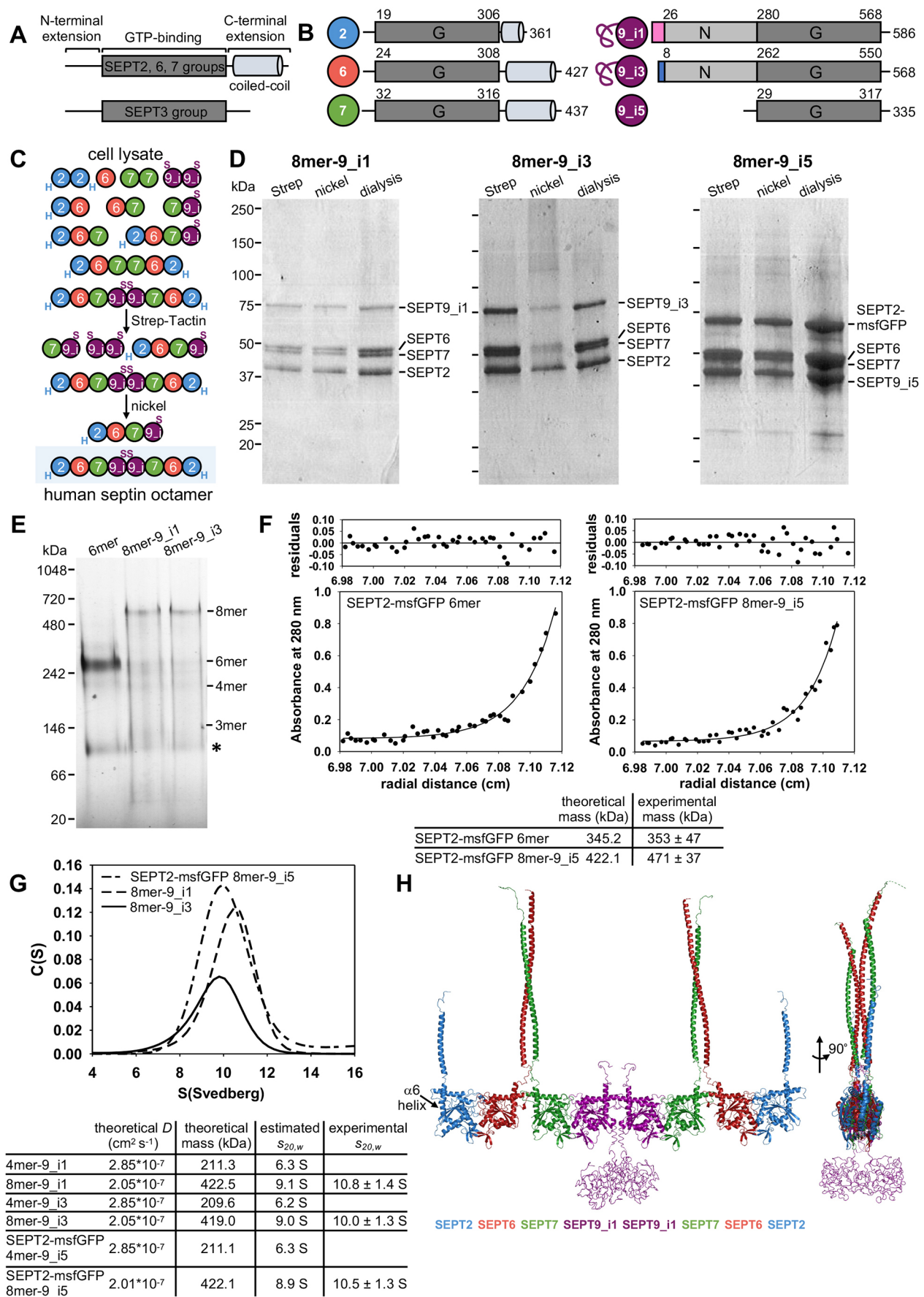


Fig. 1. See next page for legend.

Fig. 1. Isolation and characterization of recombinant human octamers containing distinct SEPT9 isoforms. (A,B) Schematic representation of a mammalian septin showing the conserved GTP-binding (G) domain flanked by N- and C-terminal extensions. There is experimental evidence that the N-terminal extension, at least for some septins, is intrinsically disordered (Garcia et al., 2006). With the exception of SEPT3 group septins, the C-terminal extension is predicted to contain a coiled-coil (A). Schematics in B depict the human septins used in this study, their size indicated by the C-terminal residue number. Residue numbers at the start and end of the G-domains correspond to the start of the $\alpha 0$ helices and the end of the $\alpha 6$ helices, respectively. Residue numbers right after the isoform-specific sequences for SEPT9_i1 and SEPT9_i3 indicate the start of their shared long N-terminal extension. The final 28 residues of this extension constitute the N-terminal extension of the short isoform, SEPT9_i5. Color-coded spheres depicting the different subunits throughout the manuscript are shown next to the respective septins. The freehand line preceding the SEPT9 G-domain of the long isoforms depicts their large N-terminal extension. (C) Schematic overview of the two-tag affinity purification scheme for isolating stoichiometric SEPT9-containing octamers. Upon septin co-expression in the bacteria cytoplasm, septins are expected to form stable hexamers and octamers (Kim et al., 2011; Sellin et al., 2011, 2014). Other hypothetical homo- and hetero-subcomplexes could also form (Kim et al., 2012; Rosa et al., 2020; Valadares et al., 2017). A first Strep-tag affinity column isolates all Strep-tagged SEPT9 complexes ('S' for Strep tag). A second nickel affinity step further isolates His₆-tagged SEPT2-containing complexes ('H' for His₆ tag), thus purifying SEPT2–SEPT6–SEPT7–SEPT9 complexes. (D) SDS-PAGE analysis of the purification of human septin octamers containing SEPT9_i1 (left, 8mer-9_i1), SEPT9_i3 (middle, 8mer-9_i3) and SEPT9_i5 (right, 8mer-9_i5). Coomassie-stained gels show fractions eluting from the Strep tag affinity column, from the nickel affinity column and after the final dialysis step. Molecular mass markers are shown on the left; the same markers were used in all gels. The 8mer-9_i1 and 8mer-9_i3 complexes shown are nonfluorescent, whereas the 8mer-9_i5 complexes shown contain msfGFP-tagged SEPT2. The identification of the bands corresponding to the different septins was based on mass spectrometry and western blot analysis (Fig. S1F). See Materials and Methods for the theoretical and apparent molecular masses. (E) Purified recombinant hexamers (6mer), 8mer-9_i1 and 8mer-9_i3 analyzed by blue native PAGE, followed by Coomassie-staining. Molecular mass markers are shown on the left. The apparent molecular masses for the recombinant 6mer and 8mer-9_i1 and -9_i3 are in line with the molecular masses of native hexamers and octamers isolated from human cell lysates (Sellin et al., 2014) (see also Materials and Methods). The theoretical sizes of SEPT2–SEPT6–SEPT7 trimers and of SEPT2–SEPT6–SEPT7–SEPT9_i1/3 tetramers are indicated as 3mer and 4mer, respectively, on the right. The asterisk points to the presence of septin monomers/dimers and the chaperone DnaK (see Materials and Methods). (F,G) Analytical ultracentrifugation of recombinant septin complexes. Sedimentation equilibrium experiments (F) of 1.5 mg ml⁻¹ of SEPT2–msfGFP 6mer (left) and SEPT2–msfGFP 8mer-9_i5 (right) at 11,000 rpm and 4°C. The filled circle symbols show the experimental radial concentration distribution at sedimentation equilibrium and the solid lines represent the best fit curves with the single-ideal species model. The residuals representing the variation between the experimental data and those generated by the fit are shown above the respective curves. The obtained experimental molecular masses (\pm s.d.) are indicated in the table below the curves. (G) shows the sedimentation coefficient distributions $c(s)$ of 0.75 mg ml⁻¹ 8mer-9_i1 (dashed line), of 0.5 mg ml⁻¹ 8mer-9_i3 (solid line) and of 1.0 mg ml⁻¹ SEPT2–msfGFP 8mer-9_i5 (twodash line) obtained from sedimentation velocity experiments at 40,000 rpm and 20°C. The experimental sedimentation coefficients $s_{20,W}$ (\pm s.d.) obtained are indicated in the table below the curves. (H) Model of a human SEPT2–SEPT6–SEPT7–SEPT9_i1–SEPT9_i3–SEPT9_i5 octamer built using coiled-coil- and homology-modeling software (see Materials and Methods for details) depicting the N-terminal extension of SEPT9_i1 as a random coil. An *en face* view (left) and a side view after a 90° rotation (right) are shown. Coiled-coils are shown to extend along the same axis as the $\alpha 6$ helix (arrow). The generated model was used to calculate the theoretical translational diffusion coefficient, D (cm² s⁻¹), and the latter to further calculate its theoretical sedimentation coefficient for comparison with the experimentally obtained one (see Materials and Methods for details). The N-terminal extensions of SEPT9_i1, SEPT9_i3 and SEPT9_i5 were all modeled as random coils in the models used in these calculations (table in G). The purification scheme (C) was used to purify at least six preparations of 8mer-9_i1, six preparations of 8mer-9_i3 and one preparation of 8mer-9_i5. SDS-PAGE (D) was performed for each preparation. Native PAGE (E) was performed for two preparations of 6mers and two preparations of each 8mer-9_i1 and 8mer-9_i3. Sedimentation equilibrium (F) was carried out for one preparation each of 6mer and 8mer-9_i5. Sedimentation velocity (G) was performed for one preparation each of 8mer-9_i1, 8mer-9_i3 and 8mer-9_i5.

His₆ tag, and the C-terminus of the central subunit, SEPT9_i, with a TEV-cleavable Strep tag. The use of a Strep-Tactin affinity column to capture Strep-tagged SEPT9_i-containing complexes, followed by a nickel affinity column to retain the SEPT9_i-containing complexes that also bear His₆-tagged SEPT2, would be expected to isolate SEPT2–SEPT6–SEPT7–SEPT9 complexes (Fig. 1C). We used this purification scheme to isolate both nonfluorescent septin complexes and fluorescent septin complexes containing SEPT2 with its C-terminus fused to monomeric superfolder GFP (msfGFP) (Costantini et al., 2012; Cranfill et al., 2016; Pedelacq et al., 2006; Zacharias et al., 2002).

Indeed, SDS-PAGE analysis of the purification of human septin complexes containing SEPT9_i1 (octamers-9_i1), SEPT9_i3 (octamers-9_i3), or SEPT9_i5 (octamers-9_i5), followed by Coomassie staining, showed that our purification scheme succeeded in isolating SEPT2–SEPT6–SEPT7–SEPT9 complexes (Fig. 1D). The assignment of the bands to the different septins was based on western blot analysis and mass spectrometry. Western blots (Fig. S1F), tryptic peptide coverage and pseudo-absolute quantitation of the mol fractions of proteins in our preparations by mass spectrometry (Fig. S1G,H) showed that the isolated complexes were >97% pure, intact and with SEPT2, SEPT6, SEPT7, SEPT9 in a 1:1:1:1 stoichiometry. We note that inverting the two columns, using batch affinity resins instead of prepacked columns, or combining prepacked columns and resins, all provided similar results (Fig. S1C–E).

Given that the purification scheme per se cannot distinguish between tetramers and octamers, we sought to determine whether the isolated SEPT2–SEPT6–SEPT7–SEPT9 complexes were composed of tetramers or/and octamers by blue native PAGE followed by Coomassie staining (Fig. 1E). For comparison, we included recombinant human SEPT2-, SEPT6-, SEPT7-containing hexamers that we isolated with the same purification protocol (Fig. S1A). Blue native PAGE has been a powerful tool for detecting the presence and relative distributions of endogenous septin complexes in cell lysates, and is able to resolve septin tetramers from hexamers and octamers (Sellin et al., 2014). Native PAGE analysis of our hexamer and octamer preparations showed bands whose size and composition were in line with the presence of intact, stoichiometric hexamers for the hexamer preparation, and intact, stoichiometric octamers for the octamer preparation, while providing no evidence for the presence of tetramers, suggesting that the latter either do not form, or they do so transiently. Our findings are consistent with SEPT9 being present in the form of stable octamers in cells (Sellin et al., 2011, 2014).

To further corroborate the presence of a stable octameric population in our preparations, we turned to analytical ultracentrifugation sedimentation equilibrium assays, comparing hexamers and SEPT9_i5-containing octamers. Sedimentation equilibrium experiments provide an experimental measure of the absolute mass of proteins in solution (Taylor et al., 2015) and thus is a powerful means of determining the species present in our preparations. The obtained molecular masses from such experiments were consistent with the presence of hexamers for the hexamer preparations, and the presence of octamers for the octamer preparations, without any detectable evidence for tetrameric complexes in the octamer preparations (Fig. 1F). We complemented these assays with analytical ultracentrifugation sedimentation velocity experiments comparing octamer-9_i1, octamer-9_i3 and octamer-9_i5 preparations (Fig. 1G). Sedimentation velocity assays measure the experimental sedimentation coefficient of proteins in solution and are thus able to detect the presence of multiple protein species. Sedimentation coefficients depend on the hydrodynamic properties

of proteins, and are directly proportional to their mass and translational diffusion coefficient, the latter including the contribution of protein shape. To interpret the obtained sedimentation coefficients and given the prediction of C-terminal coiled-coils for SEPT2, SEPT6 and SEPT7 (de Almeida Marques et al., 2012; Low and Macara, 2006; Sala et al., 2016) (Fig. 1A,B), we used coiled-coil modeling and homology-modeling software to build models of the SEPT2–SEPT6–SEPT7–SEPT9–SEPT9–SEPT7–SEPT6–SEPT2 octamers. Owing to the considerable size (~27 kDa) of the N-terminal extensions in the long SEPT9 isoforms (SEPT9_i1, SEPT9_i3) and thus their impact on the sedimentation behavior of the respective complexes, we included these in the models. Given the absence of structural homologs and given secondary structure predictions of disorder for this region (using Quick2D), we modeled the N-terminal extensions of SEPT9 as random coils (Fig. 1H; Fig. S4A) (see Materials and Methods). The short (~20–30-residue) N-terminal extensions of SEPT2, SEPT6 and SEPT7 were not included in the models. We used these model structures together with the Svedberg equation and the HullRad algorithm (Fleming and Fleming, 2018), which calculates hydrodynamic properties of molecules from their structures, to

obtain the theoretical diffusion coefficients of octamers and tetramers, as well as their theoretical sedimentation coefficients (table in Fig. 1G; see Materials and Methods for details). The experimental sedimentation coefficients for all octamers-9_i1, octamers-9_i3 and octamers-9_i5 were in excellent agreement with the ones estimated from the model structures, with the sedimentation coefficient distributions again providing no evidence for the presence of tetramers that are expected to sediment much more slowly, with a difference of ~3S.

Single-particle electron microscopy analysis of recombinant septin octamers reveals the flexibility of N- and C-terminal extensions, and provides evidence for SEPT2 occupying the end positions

To visualize the isolated octamers, we employed single-particle electron microscopy (EM) of negative-stained octamer preparations in a high-salt buffer (300 mM KCl) to prevent septin complexes from polymerizing. Low-magnification EM images of negative-stained octamer preparations highlighted the rod-like appearance of the complexes (Fig. 2A). Single particles in such fields, typically ~3,000–4,000 particles, were computationally aligned

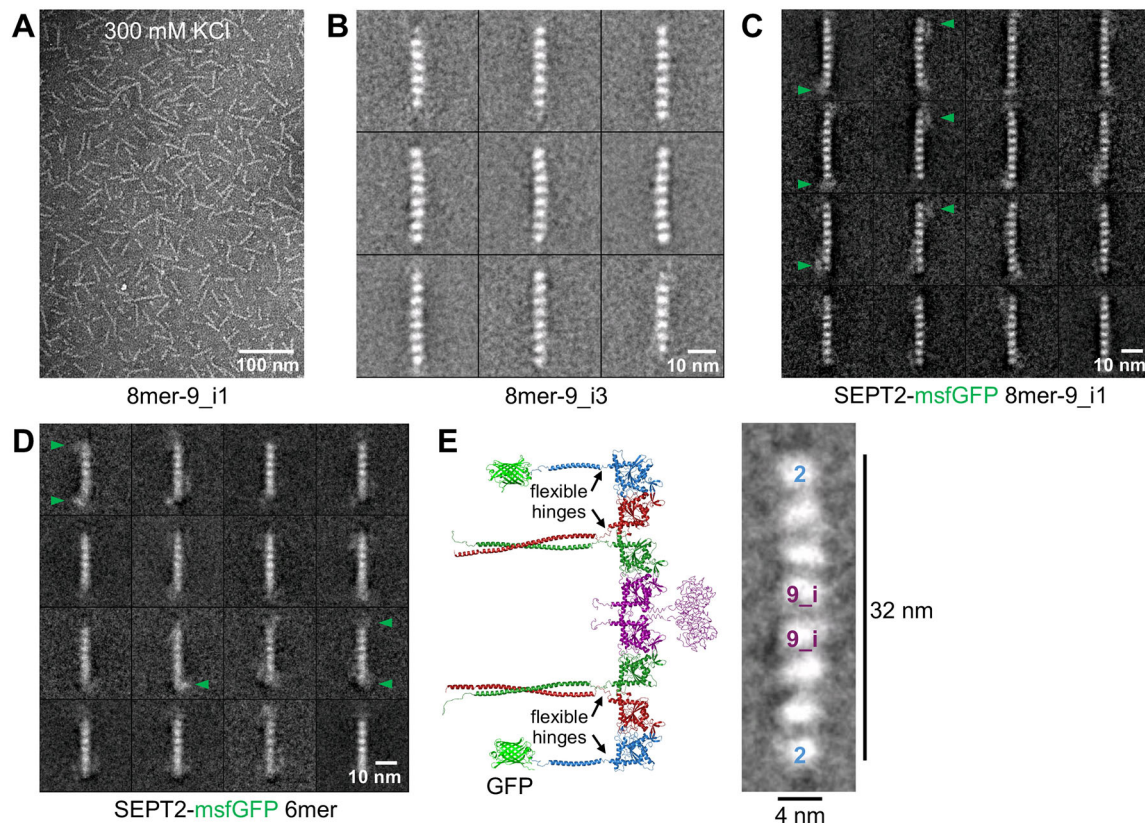


Fig. 2. Electron microscopy analysis of recombinant SEPT9-containing octamers. (A) Negative-stain EM image of recombinant 8mer-9_i1 at 25 nM in a high-salt buffer (300 mM KCl) showing the rod-like appearance of the complexes. (B–D) Single-particle EM analysis of recombinant septin complexes. Each panel shows a gallery of representative class averages (~100 particles each) derived from the processing of ~3000–4000 particles from micrographs of negative-stained complexes, as in A (see Materials and Methods for details). All class averages for 8mer-9_i3 complexes (B) exhibited a rod shape with no evidence of additional densities at their ends (or along their sides, consistent with a high degree of flexibility for the coiled-coils of SEPT2, SEPT6 and SEPT7, and in line with the absence of secondary structure prediction for the large (27-kDa) N-terminus of the long SEPT9 isoforms. Class averages of SEPT2–msfGFP 8mer-9_i1 (C) and of SEPT2–msfGFP 6mer (D) displayed additional densities at one or both ends of the rods (green arrowheads), indicating that SEPT2 occupies the termini of 6mer and 8mer. The fuzzy density of the C-terminal GFP and its multiple positions around the end subunit suggest an intrinsic orientational flexibility in the junction between the G domain and the coiled-coils of SEPT2. (E) Juxtaposition of a model of the octamer-9_i1 (Fig. 1H), also containing SEPT2–msfGFP, with a high magnification class average image of an octamer from B. All septin complexes shown contain full-length, human septins apart from B, which depicts an example of mammalian septin octamers-9_i3 containing mouse SEPT2-, human SEPT6-, human SEPT7ΔN19 and human SEPT9_i3 (see Materials and Methods).

and classified into classes with distinct features (for example, orientation, curvature or number of subunits). Each class typically contained ~50–100 particles (see Materials and Methods). Fig. 2B shows a gallery of class averages for octamers-9_i3. Each image is the average of all the particles in a given class, and has an increased signal to noise ratio compared to the raw images, which allows us to distinguish individual septin subunits within the octameric complex. All class averages for octamers-9_i3 exhibited a characteristic rod shape, similar to what has been seen for recombinant human/mammalian septins (Mavrakakis et al., 2016; Mendonca et al., 2019; Sirajuddin et al., 2007) or septins isolated from mammalian cell lines and tissues (Hsu et al., 1998; Kim et al., 2011; Kinoshita et al., 2002; Sellin et al., 2011; Soroor et al., 2021), and in line with rod-shaped septin complexes from other species, including budding yeast (Bertin et al., 2008; Frazier et al., 1998; Garcia et al., 2011; Taveneau et al., 2020), *C. elegans* (John et al., 2007) and *Drosophila* (Akhmetova et al., 2015; Field et al., 1996; Mavrakakis et al., 2014). The class averages did not show additional densities at their ends or along their sides, suggesting an intrinsic orientational flexibility in the junction between the G-domain and the coiled-coils of SEPT2, SEPT6 and SEPT7, whose densities are averaged out in such analysis. Such flexibility for the coiled-coils, deduced from the absence of electron density in the crystal structure of the SEPT2–SEPT6–SEPT7 trimer (PDB ID: 2QAG; Sirajuddin et al., 2007) and the absence of additional densities in single particle EM of budding yeast, mammalian, *C. elegans* and *Drosophila* complexes (Bertin et al., 2008; Garcia et al., 2011; John et al., 2007; Mavrakakis et al., 2014, 2016; Mendonca et al., 2019; Taveneau et al., 2020), seems to be a general feature of septins. Moreover, there was no density that could be assigned to the large (~27-kDa) N-terminus of the long isoforms, in line with secondary structure predictions of disorder for this region.

Class averages of SEPT2–msfGFP octamers-9_i1 (Fig. 2C) did display additional densities at one or both ends of the rods (green arrowheads), indicating that the GFP-tagged SEPT2 subunits occupy the termini of octamers. The same observation was made with SEPT2–msfGFP-containing hexamers (Fig. 2D). The fuzzy density of the C-terminal GFP and its multiple positions around SEPT2 again point to a flexible hinge region between the last helix of the G-domain ($\alpha 6$ helix, Fig. 1H) and the coiled-coils of SEPT2 (Fig. 2E).

Recombinant septin octamers harboring SEPT9_i1, SEPT9_i3 or SEPT9_i5 polymerize into higher-order filament assemblies in solution

In addition to SEPT2 at the ends of octamers, whose presence is determining for octamer polymerization in solution, other structural elements such as the N- or C-terminal extensions could also impact septin filament assembly (Bertin et al., 2010). To test the effect of the SEPT9-specific N-terminal extension on septin polymerization in solution, we compared octamers containing either a long or a short SEPT9 isoform. To this end, octamers-9_i1, -9_i3 and -9_i5 were either dialyzed or diluted into a low-salt buffer (50 mM KCl). The resulting assemblies were observed with spinning disk fluorescence microscopy on poly(L-lysine)-poly(ethylene glycol) (PLL-PEG) passivated glass using SEPT2–msfGFP-containing octamers (Fig. S2A–C), and examined at higher spatial resolution by negative-stain EM using nonfluorescent or SEPT2–msfGFP-containing octamers (Fig. 3A–C). Both octamers with a long or a short SEPT9 isoform polymerized into higher-order filament assemblies. Fluorescence microscopy revealed a variety of assembly morphologies; optical sectioning showed that all octamers assembled into interconnected and/or branched

networks of straight and curved filament bundles extending along 10–50 μm in the xy plane and by 10–50 μm in the z plane (Movie 1 shows a representative z -stack; Fig. S2A–C shows maximum-intensity projections of z -stacks). Octamers could organize into straight bundles (left panel in Fig. S2B,C), but also into what looked like highly convoluted filamentous assemblies (Fig. S2A, right panel in Fig. S2B). Measurements of isolated septin filament bundles in solution for octamers-9_i3 and -9_i5 (left panel in Fig. S2B,C) showed that they could reach up to ~5–8 μm in length.

Negative-stain EM similarly revealed a variety of filamentous assemblies. Octamers-9_i1 could organize into isolated or interconnected straight or slightly curved bundles (Fig. 3Ai,ii), and into networks of interconnected, highly convoluted and ring-forming filament bundles (Fig. 3Aiii–v) corresponding to the similarly convoluted filamentous assemblies observed by fluorescence microscopy (Fig. S2A). Septin filament bundles were a few micrometers long and ~50–150 nm in width (Fig. S2H). High magnifications of regions within the filament bundles (red-outlined insets in Fig. 3A) revealed that bundles were made of single septin filaments (blue arrowheads in Fig. 3A and measurements of septin filament width in Fig. S2H) running parallel to each other, with septin filaments within bundles occasionally looking paired (orange arrowheads in Fig. 3A). Given the high density of filaments and the 2D projection character of negative-stain EM, we cannot conclude whether these are truly paired filaments like budding yeast septin filament pairs (Bertin et al., 2008); if so, these would have to be more tightly paired given their narrow interfibril spacing (~5 nm). Similarly narrow interfibril spacing has been observed recently for paired filaments formed by human septin hexamers in solution (Leonardo et al., 2021) and by membrane-bound *Drosophila* septin hexamers (Szuba et al., 2021). Septin filament bundles exhibited a high degree of interconnectivity, with a given bundle often showing splayed ends that could connect to one or more different bundles, or with septin filaments forming meshes (Fig. 3Av). We speculate that the exposed, flexible coiled-coil-containing C-terminal extensions, and potentially the long N-terminal extensions of SEPT9, drive the interconnections in the higher-order assemblies we observe. Octamers-9_i3 also formed filament bundles (Fig. 3Bi) and what appeared to be paired filaments, again with narrower interfibril spacing (~5 nm) than those observed for budding yeast septin filament pairs in solution (~10 nm) (Bertin et al., 2008) (Fig. 3Bii). Octamers-9_i3 additionally formed wheel-like structures associating with the bundles (Fig. 3Bi, green arrowheads). These wheels had a diameter of 20–30 nm and could correspond to two or three octamer rods connected end-to-end, forming the circumference of the wheels; the interior of the wheels appeared to contain electron density. Very similar-looking wheels of similar dimensions have been reported for budding yeast Shs1-containing octamers, with the electron density in their interior attributed to the C-terminal coiled-coils stabilizing these structures (Garcia et al., 2011; Taveneau et al., 2020). Coiled-coils in the interior of octamer-9_i3 wheels could similarly stabilize these structures, whose formation would require substantial bending of the octamers. Octamers-9_i5 also formed filaments (Fig. 3C), although the high density in these EM samples did not allow us to deduce whether these were single or intertwined/paired filaments. Our combined observations from fluorescence and EM show that recombinant octamers with either a long or a short SEPT9 isoform form higher-order filament assemblies.

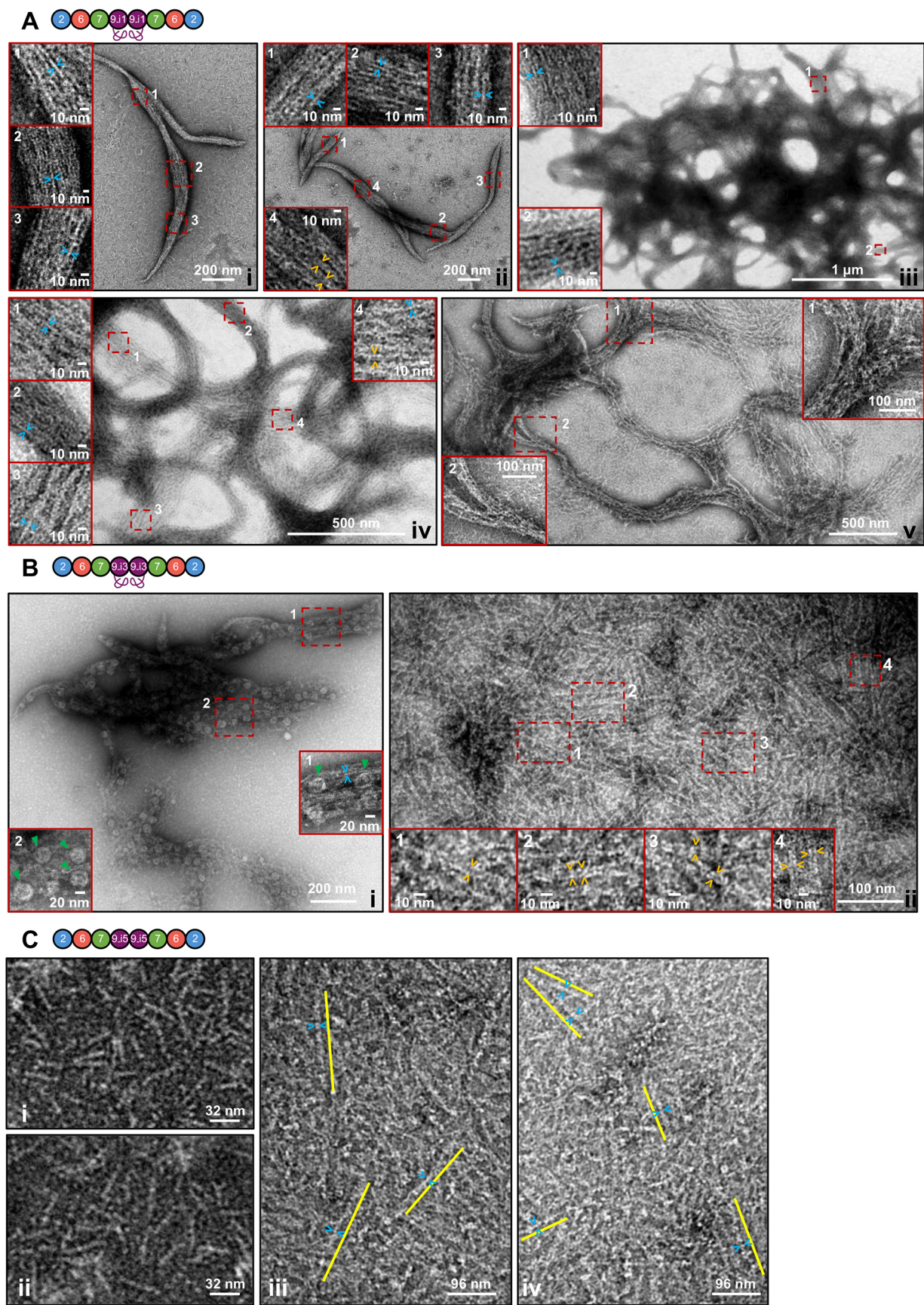


Fig. 3. See next page for legend.

Fig. 3. *In vitro* reconstitution of septin polymerization in solution using recombinant septin octamers with distinct SEPT9 isoforms. (A) Negative-stain EM images of higher-order filament assemblies upon polymerization of 8mer-9_i1 at low salt (50 mM KCl). 8mer-9_i1 were polymerized at 1 μ M (Ai,ii) or 0.2 μ M (Aiii–v) final octamer concentration. The insets show magnifications of selected regions of interest (dashed rectangles in red), and highlight single septin filaments (blue arrowheads), septin filaments that are possible pairs (orange arrowheads), and splayed filament bundles (v). (B) Negative-stain EM images of higher-order filament assemblies upon polymerization of 8mer-9_i3 at low salt (50 mM KCl). 8mer-9_i3 were polymerized at 0.2 μ M final octamer concentration. The insets show magnifications of selected regions of interest (dashed rectangles in red), and highlight single septin filaments (blue arrowheads), paired septin filaments (orange arrowheads), and wheel-like structures whose perimeter corresponds to two or three octamers connected end to end (green arrowheads). (C) Negative-stain EM images of higher-order filament assemblies upon polymerization of 8mer-9_i5 at low salt (50 mM KCl). 8mer-9_i5 were polymerized at 0.1 μ M (Ci,ii) or 0.25 μ M (Ciii–v) final octamer concentration. Regions with single octamers (~32 nm long) are shown in i, ii. Densely covered regions with septin filaments are shown in iii; iv, examples of filaments (blue arrowheads) composed of three (~96 nm long) to nine octamers are shown with yellow lines running parallel to the filaments. All septin complexes shown contain full-length, human septins apart from those in the left panel in B, which depicts an example of mammalian septin octamers-9_i3 containing mouse SEPT2-, human SEPT6-, human SEPT7 Δ N19 and human SEPT9_i3 (see Materials and Methods).

For comparison, we examined human septin hexamers, mammalian septin hexamers (containing mouse SEPT2, human SEPT6 and human SEPT7 Δ N19), and *Drosophila* hexamers whose polymerization was characterized previously (Mavrikis et al., 2014; Mavrikis et al., 2016). Fluorescence microscopy and negative-stain EM of human, mammalian and *Drosophila* hexamers in a low-salt buffer (Fig. S2D–G) showed that human and mammalian hexamers organized in a very similar manner into straight and curved filament bundles made of single and possibly paired septin filaments (Fig. S2F,G,H). *Drosophila* hexamers organized in characteristic needle-like bundles, as reported previously (Mavrikis et al., 2014; Mavrikis et al., 2016), which were not as heavily interconnected as their human counterparts. Human hexamer and octamer bundles displayed similar lengths and widths (Fig. S2H, see legend for median values).

Recombinant octamers-9_i1, octamers-9_i3 and octamers-9_i5 bind and cross-link actin filaments in solution

Septins are thought to interact with actin filaments either indirectly, via myosin-II (Joo et al., 2007), or directly. The possibility of direct interactions between septin hexamers and actin filaments was raised by reconstitution assays showing that recombinant mammalian and *Drosophila* hexamers bind and cross-link actin filaments into bundles (Mavrikis et al., 2014). Given that, in cells, both of the long isoforms, SEPT9_i1 and SEPT9_i3, and the short isoform SEPT9_i5 associate with the actin cytoskeleton (Connolly et al., 2011; Dolat et al., 2014b; Kim et al., 2011; Surka et al., 2002; Verdier-Pinard et al., 2017), we sought to test whether recombinant octamers-9_i1, -9_i3 and -9_i5 have the capacity to directly bind and cross-link actin filaments, as hexamers do, and if so, whether the presence of a specific SEPT9 isoform makes any difference.

To this end, we used spinning disk fluorescence microscopy to image dilute solutions (1 μ M) of single actin filaments on PLL-PEG passivated glass, after spontaneous polymerization of purified rabbit muscle G-actin in the presence or absence of nonfluorescent or SEPT2–msfGFP-containing octamers-9_i1, -9_i3 and -9_i5 (Fig. 4A–E). In the absence of octamers, fluorescence microscopy showed isolated fluctuating single actin filaments, as expected (Fig. 4A; Movie 2). In the presence of 0.3 μ M

SEPT2–msfGFP-containing octamers-9_i1 (Fig. 4C), octamers-9_i3 (Fig. 4D), or octamers-9_i5 (Fig. 4E), fluorescence microscopy revealed actin filaments cross-linked into straight and curved bundles, in a very similar manner for all three types of octamers, and very similarly to cross-linking induced by human, mammalian and *Drosophila* hexamers (Fig. S3A–C and Mavrikis et al., 2014). Actin filament cross-linking was observed for septin concentrations of 20–30 nM and above, with identical results obtained with nonfluorescent septins (data not shown). The images shown in Fig. 4C–E were typically captured a few hours into actin polymerization or after overnight incubation, and show the coexistence of straight and curved actin filament bundles, either as isolated bundles or bundles connected to each other forming networks. Thicker actin bundles, corresponding to a brighter signal in the actin channel, fluctuated very little, suggesting that they were rigid, whereas thinner actin bundles and single actin filaments, emanating from the ends or the sides of bundles, or connecting neighboring bundles, were freely fluctuating (Movie 3). Septins systematically colocalized with the actin bundles, indicative of their actin filament cross-linking activity (right panels in Fig. 4C–E depict magnified views of selected red-outlined regions on the left). Saturating the actin and septin channels to bring out features with weaker signals, notably single actin filaments (arrowheads in the actin channel in Fig. 4C–E), revealed that septins localized only to actin bundles and not to single actin filaments, suggesting cooperativity in septin–actin binding. Such cooperativity has also been reported for other actin filament cross-linkers (Winkelman et al., 2016).

DISCUSSION

In summary, our study describes the first isolation and characterization of recombinant human SEPT2–SEPT6–SEPT7–SEPT9–SEPT9–SEPT7–SEPT6–SEPT2 octamers containing distinct long or short SEPT9 isoforms. The employed two-tag purification scheme is rapid, taking one full day starting from bacteria lysis, works with prepacked columns, batch resins or combinations thereof, thus providing flexibility, and yields ~1–3 mg of purified octamers (a few hundreds of microliters in the micromolar concentration range) from a starting 3.5–5 l of culture, enabling biochemical and biophysical reconstitution studies at physiological septin concentrations. A combination of biochemical and biophysical assays confirmed the octameric nature of the isolated complexes in solution, and also provided evidence for SEPT2 occupying the end positions in the octamer, in agreement with recent studies on septin positioning in recombinant human hexamers (Mendonca et al., 2019), recombinant SEPT3-containing octamers (DeRose et al., 2020) and SEPT9-containing octamers isolated from cell lysates (Soroor et al., 2021).

Recombinant octamers with either a long or a short SEPT9 isoform were competent for polymerization in solution, in line with studies of SEPT9-containing octamers isolated from cell lysates (Soroor et al., 2021). The observation of a large variety in the morphologies of filament assemblies in solution could result from several factors. In this study we examined septin assembly using recombinant octamers bound to the endogenous GDP/GTP in the bacterial cytoplasm, without the exogenous addition of nucleotide during cell lysis or post purification; it is conceivable that regulation of the GDP/GTP state of septins in cells regulates their higher-order assembly (Weems and McMurray, 2017). A further important element is that interactions of septins with membranes, accessory proteins, or the actin and/or microtubule cytoskeleton could influence their assembly in cells. Our observations lead us to speculate that, in the absence of any other interacting surface or

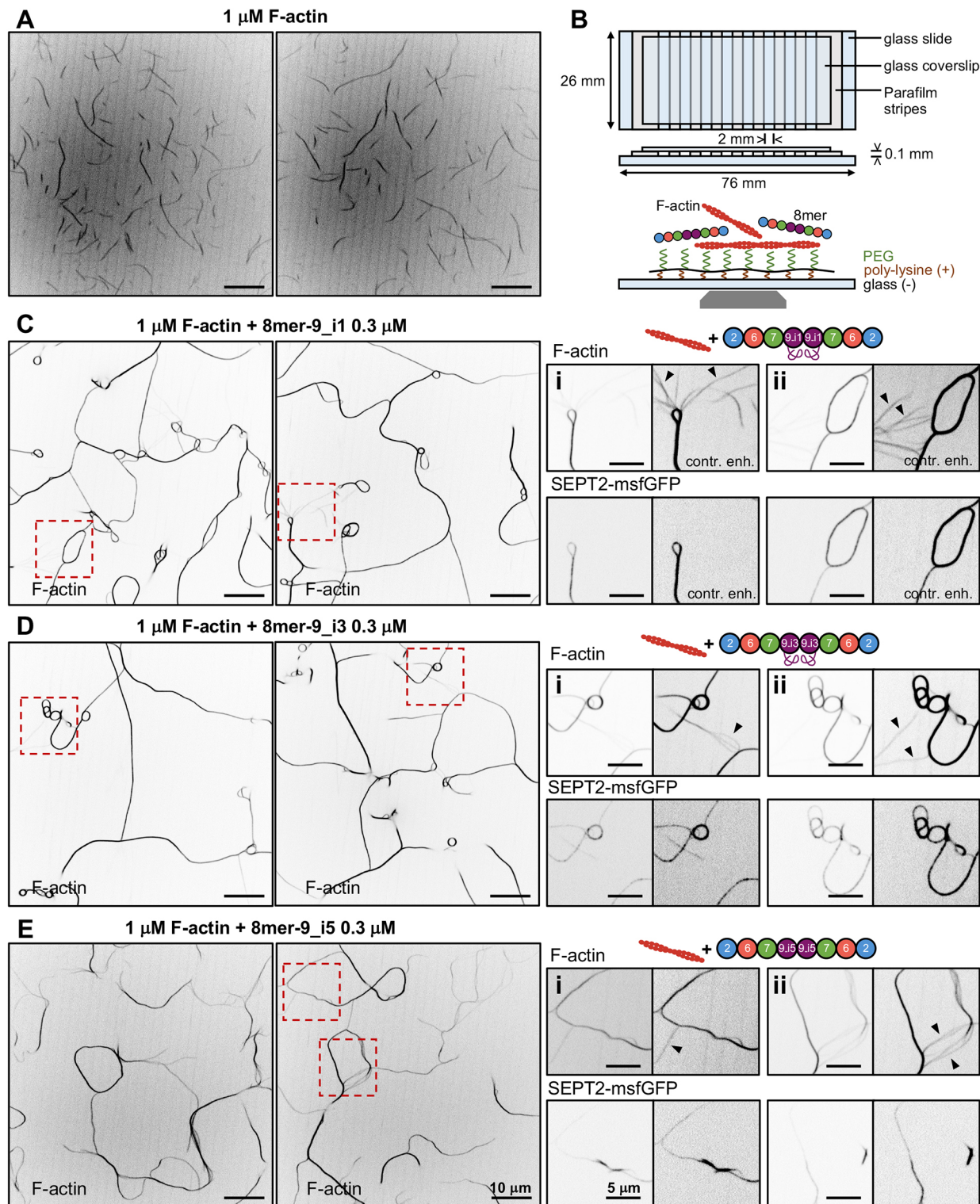


Fig. 4. See next page for legend.

protein, higher-order septin assembly is dominated by the exposed, flexible coiled-coil-containing C-terminal extensions and/or the N-terminal extensions, resulting in the high plasticity and polymorphism we observe. The potentially disordered N-terminal extensions of SEPT9 could conceivably become structured (Fig. S4D–F) in the presence of interacting surfaces and binding partners, for example, cell membranes and the actin or microtubule

cytoskeleton, resulting in a narrower range of assembly geometries. The filamentous assemblies we observe in solution could reflect the higher-order filamentous septin assemblies that have been observed in the cytosol of cells upon perturbation of interacting partners, for example, upon disruption of actin stress fibers (Joo et al., 2007; Kim et al., 2011; Kinoshita et al., 2002, 1997; Xie et al., 1999).

Fig. 4. *In vitro* reconstitution of actin filament cross-linking by recombinant human septin octamers with distinct SEPT9 isoforms. (A,B) Representative spinning disk fluorescence images of reconstituted, fluctuating single actin filaments (A) upon spontaneous polymerization of G-actin at 1 μ M on PLL-PEG-passivated glass in a flow chamber constructed as shown in B (see Materials and Methods for details). Actin filaments are visualized by including Alexa Fluor 568-conjugated phalloidin during polymerization. The time-lapse sequence containing the still image shown on the left panel of A is shown in Movie 2. (C–E) Representative spinning disk fluorescence images of reconstituted actin filaments, prepared as in A, and polymerized in the presence of 8mer-9_i1 (C), 8mer-9_i3 (D), or 8mer-9_i5 (E). Actin filaments are visualized with Alexa Fluor 568-conjugated phalloidin, and septins with SEPT2–msfGFP. Two examples of large fields of view are shown for each, depicting the similar cross-linking of actin filaments into actin filament bundles in the presence of all three types of octamers; only actin labeling is shown. A time-lapse sequence containing the still image shown on the right panel of C is shown in Movie 3. Insets on the right side of each panel show higher magnifications of selected regions of interest on the left (dashed squares in red). Two regions of interest (i,ii) are shown in each case, depicting both the actin (top row) and septin (bottom row) signals. For each inset, actin and septin signals are shown in duplicates: the first set shows the raw signals without any saturation, whereas the second set, adjacent to the first one, shows both actin and septin signals after deliberate contrast enhancement. The contrast-enhanced images in the actin channel saturate the actin bundles, while bringing out weaker-intensity single actin filaments (black arrowheads). The respective contrast-enhanced images in the septin channel show the presence of septins in actin bundles, but their absence from single actin filaments. Scale bars: 10 μ m (all large fields of views), 5 μ m (insets). All images shown use an inverted grayscale.

Octamers isolated from mammalian cell lysates bearing short SEPT9 isoforms were more frequently observed as bundled filaments while the ones bearing long SEPT9 isoforms were frequently single filaments (Soroor et al., 2021). There are two main differences between the recombinant human septin octamers isolated in our study and octamers immunopurified from cell lysates that could explain differences in their higher-order filament assemblies. First, recombinant octamers have a defined septin composition (in this case containing exclusively SEPT2, SEPT6, SEPT7 and SEPT9), whereas immunopurified octamers using tagged SEPT9 as a bait can contain additional septins (for example, SEPT11 in Soroor et al., 2021). Second, differences in post-translational modifications (for example septin phosphorylation and SUMOylation) in the different expression systems can have a major impact on higher-order filament assembly (Estey et al., 2013; Ribet et al., 2017). Understanding how specific septins contribute to higher-order filament assembly and how post-translational modifications regulate human septin assembly constitute challenges for future studies.

Recombinant human octamers-9_i1, -9_i3 and -9_i5 all shared the capacity to cross-link actin filaments. The similarities with the actin filament cross-linking capacity of human hexamers raise the possibility that SEPT9, in the context of an octameric complex, does not contribute to actin filament cross-linking, but we cannot exclude such a contribution (Dolat et al., 2014b; Smith et al., 2015). In the latter case, the contribution of SEPT9 to actin filament cross-linking seems to be indistinguishable from that of the other septins in the complex. Future studies of how short and long SEPT9 isoforms differ with respect to their interactions with actin filaments will help provide insights into their different functional contributions in cells. Our observations raise the possibility that septin-decorated actin structures such as stress fibers and the cytokinetic ring reflect direct interactions between actin filaments and hexameric or/and octameric septin complexes.

Given the importance of SEPT9 in mammalian physiology and disease, the isolation of recombinant human septin octamers

bearing distinct SEPT9 isoforms will facilitate studies of SEPT9 in the physiological context of its assembly into hetero-octamers. Septins engage in multiple interactions, making it difficult to dissect their function in the complex environment of the cell. Cell-free reconstitution studies with SEPT9-containing octamers and candidate interacting partners thus provide a powerful complementary approach to cellular and animal model studies for exploring human septin function.

MATERIALS AND METHODS

Plasmids and cloning

We refer to the mammalian septin protein products as SEPT2, SEPT6, SEPT7 and SEPT9 (SEPT9_i to denote isoforms; the longest isoform being i1, the next longest i2, and so on), nonitalicized and with all letters capitalized, according to the mammalian septin nomenclature established by Hall et al. (2008) and Macara et al. (2002). Human septin gene symbols are italicized with all capital letters, and mouse septin gene symbols italicized with their first letter capitalized. Mouse SEPT2, human SEPT6 and human SEPT7 Δ N19 cDNAs were originally obtained from Alfred Wittinghofer (Max Planck Institute of Molecular Physiology, Germany) and used for the expression and purification of recombinant mammalian SEPT2-, SEPT6- and SEPT7-containing hexamers bearing TEV-cleavable His₆ N-terminally-tagged mouse SEPT2, human SEPT6 and noncleavable Strep-tag-II C-terminally-tagged human SEPT7 Δ N19 (Figs S2G and S3C) (Mavrikis et al., 2014). Human SEPT9_i1 cDNA was a gift from Cristina Montagna (Albert Einstein College of Medicine, USA). Human SEPT9_i3 cDNA was a gift from William Trimble (University of Toronto, Canada). Both human SEPT9_i1 and SEPT9_i3 cDNAs have a valine at position 576 for SEPT9_i1 and 558 for SEPT9_i3 instead of a methionine, compared to the respective sequences in UNIPROT (identifiers Q9UHD8-1 and Q9UHD8-2); a valine in that position is found in several human clones and many other primates suggesting this is a polymorphism. We used the pET-MCN vectors pNEA-vH (pET15b backbone) and pNCS (pCDF-DuET backbone) for subcloning (Diebold et al., 2011).

Building on our cloning strategy for generating hexamers and with the plasmids available at the time (Mavrikis et al., 2014, 2016), we initially generated a bicistronic pNEA-vH vector for co-expression of TEV-cleavable His₆ N-terminally-tagged mouse SEPT2 and human SEPT6, and a bicistronic pNCS vector for co-expression of human SEPT7 Δ N19 and noncleavable Strep-tag-II C-terminally-tagged human SEPT9_i3. To this end, we digested human SEPT6 in pNCS with SpeI/XbaI, ligated the insert to SpeI-digested mouse SEPT2 in pNEA-vH and selected the clones with the correct insert orientation using restriction analysis. Similarly, we digested human SEPT9_i3 in pNCS with SpeI/XbaI, ligated the insert to SpeI-digested human SEPT7 Δ N19 in pNCS and selected the clones with the correct insert orientation using restriction analysis. The combination of these vectors was used to produce and purify recombinant mammalian SEPT9_i3-containing octamers bearing TEV-cleavable His₆ N-terminally-tagged mouse SEPT2, human SEPT6, human SEPT7 Δ N19 and noncleavable Strep-tag-II C-terminally-tagged human SEPT9_i3 (Fig. 2B; left panel in Fig. 3B).

To introduce a TEV cleavage site for Strep-tagged SEPT9_i3 and also generate SEPT9_i1 and SEPT9_i5-containing octamers, and to introduce the missing N-terminal 19 residues in SEPT7 (Fig. S1B), SEPT7 Δ N19 being initially erroneously annotated as full-length (Macara et al., 2002), we proceeded as follows. To generate full-length human SEPT7 (UNIPROT identifier Q1681-1), we linearized the pNCS plasmid with NdeI/NheI and employed seamless cloning (In-Fusion HD Cloning Plus Kit from Takara Bio, Cat. #638910) with the following primers: forward 5'-AAGGAGATACATATGTCGGT-CAGTGCGAGATCCGCTGCTGCTGAGGAGAGGAGCGTCAACAG-CAGCACCATTGGTAGCTCAACAGAAGAACCCTTG-3' and reverse 5'-GCAGCCTAGGGCTAGCTCTAGACTATTAGGATCCTTAAAGATCT-TCCCTTTCTTCTGTTCTTTTCC-3'. To insert human SEPT9_i1, SEPT9_i3, and SEPT9_i5 with a TEV-cleavable C-terminal Strep-tag-II upstream of SEPT7, we linearized the SEPT7-containing plasmid with SpeI and used seamless cloning with the following primers: forward

5'-ACAATTCCTCCACTAGTAATAATTTTGTCTTAACCTTAAAGAAGGA-GATATACATGAAGAAGTCT-3' for SEPT9_i1, forward 5'-ACAATTCCTCCACTAGTAATAATTTTGTCTTAACCTTAAAGAAGGAGATATAC-AtATGGAGAGG-3' for SEPT9_i3 and forward 5'-ACAATTCCTCCACTAGTAATAATTTTGTCTTAACCTTAAAGAAGGAGATATACATATGGCCGACACCCAG-3' for SEPT9_i5 and reverse 5'-CAAAATTATTACTAGTTATTTTTCGAACTGCGGGTGGCTCCAGC-CGCTGCCGTGCCCTGGAAGTAAAGGTTTTCCATCTCTGGGGCT-TCTGGC-3', thus generating bicistronic pncS vectors for co-expression of full-length human SEPT7 and human SEPT9_i (Fig. S1A,B).

Mouse and human SEPT2 differ in five residues (I67V, S207N, S352G, S354G, Q359H, the latter residue being human), presenting 98.61% identity. To replace mouse SEPT2 with human SEPT2 in the bicistronic pncS vector for co-expression of TEV-cleavable His₆ N-terminally-tagged mouse SEPT2 and human SEPT6 (Fig. S1A,B), we linearized pncS-vH with KpnI/NheI and employed seamless cloning with the following primers: forward 5'-ATCATCACAGCAGCGGTACCGGCAG-CGGCGAAAACCTTTACTTCCAGGGCCATATGTCTAAGCAACAAC-CAACTCAGTTTATAAATC-3' and reverse 5'-ATCTCCTAGGGC-TAGTCTAGACTATTAGGATCCTCACACATGGTGGCCGAGAG-3'.

The human SEPT2 cDNA contains several restriction sites routinely used in cloning (KpnI, NheI and BamHI), and to facilitate subsequent subcloning using these sites, we chose to generate a synthetic human SEPT2 coding sequence (Eurofins Genomics, Germany) that employs the codon usage of mouse SEPT2 (which does not contain the mentioned restriction sites) except for the five codons that differ between the two species, for which we used codons encoding the human residues V67, N207, G352, G354 and H359.

To produce fluorescent octamers, we swapped SEPT2 in the dual expression vector for SEPT2 with its C-terminus tagged with monomeric (V206K) superfolder GFP (msfGFP) (no linker sequence). We generated a synthetic msfGFP coding sequence (Eurofins Genomics, Germany), linearized the dual expression pncS-vH plasmid with KpnI/NheI and employed two-insert seamless cloning with the following primers: forward 5'-ATCATCACAGCAGCGGTACCGGCAGCGGCGAAAACCTTTACT-TCCAGGGCCATATGTCTAAGCAACAACCACTCAGTTTATAAATC-3' and reverse 5'-TTGGACACCATGCTGGCCGAGAGC-3' for SEPT2, and forward 5'-CCATGTGGTGTCCAAGGGCGAGGAGC-3' and reverse 5'-ATCTCCTAGGGCTAGCTAGACTATTAGGATCCTTACTTGTA-AGTCTATCCATGCCAG-3' for msfGFP.

To generate recombinant human hexamers bearing TEV-cleavable His₆ N-terminally-tagged human SEPT2, human SEPT6 and TEV-cleavable Strep-tag-II C-terminally-tagged human SEPT7 (Fig. S1A,B, Fig. S2D,F, Fig. S3A) we employed a similar cloning strategy. To insert human SEPT2 or human SEPT2-msfGFP in the pncS-vH vector, we linearized pncS-vH with KpnI/NheI and employed seamless cloning with the same primers used above in the context of the dual vector. To generate TEV-cleavable Strep-tag-II C-terminally-tagged full-length human SEPT7, we linearized the pncS plasmid with NdeI/NheI and employed seamless cloning with the following primers: forward 5'-AAGGAGATATACATATGTCGGTCA-GTGCAGATCCGCTGCTGTGAGGAGAGGAGCGTCAACAGCAG-CACCATGGTAGCTCAACAGAAGAACCTTG-3' and reverse 5'-GCAGCCTAGGGCTAGCTCTAGACTATTAGGATCCTTATTTTCGA-ACTGCGGGTGGCTCCAGCCGCTGCCGTGCCCTGGAAGTAAAG-GTTTTCAAAGATCTTCCCTTTCTTCTTGTCTTTTCC-3'. To insert human SEPT6 upstream of SEPT7, we linearized the SEPT7-containing plasmid with SpeI and used seamless cloning with the following primers: forward 5'-ACAATTCCTCCACTAGTAATAATTTTGTCTTAACCTTAA-GAAGGAGATATACATATGGCAGCGACCGATATAGC-3' and reverse 5'-CAAAATTATTACTAGTCTATTAGGATCCTTAATTTTCTTCTCT-TTGCTCTCTTCAGAGTCTGTGAG-3', thus generating a bicistronic pncS vectors for co-expression of human SEPT6 and full-length human SEPT7.

Recombinant *Drosophila* hexamers bearing TEV-cleavable His₆ N-terminally-tagged DSep1, and untagged or mEGFP N-terminally-tagged DSep2 and noncleavable Strep-tag-II C-terminally-tagged Peanut were described previously (Fig. S2E) (Mavrakis et al., 2014, 2016). To generate *Drosophila* hexamers along the lines of the human ones, i.e., with a TEV-

cleavable Strep-tag for Peanut and with the C-terminus of DSep1, the homolog of human SEPT2, tagged with msfGFP (Fig. S2E; Fig. S3B), we proceeded as follows. To insert DSep1-msfGFP in the pncS-vH vector, we linearized pncS-vH with NdeI/BamHI and employed two-insert seamless cloning with the following primers: forward 5'-ACTTCCAGGGCCATATGGCCGATACAAAGGGCTTTTC-3' and reverse 5'-TTGGACACCTGCTGGGCTGCATGC-3' for DSep1, and forward 5'-CCAGCAGGTGTCCAAGGGCGAGGAGC-3' and reverse 5'-TAGACTATTAGGATCCTTACTTGTACAGCTCATCCATGCCAG-3' for msfGFP. To introduce the TEV cleavage site for Peanut in the bicistronic pncS vector for co-expression with DSep2, we linearized the dual expression pncS plasmid with NcoI/NheI and employed seamless cloning with the following primers: forward 5'-CGCCAGAAGCCCATGGAG-3' and reverse 5'-GCAGCCTAGGGCTAGCTCTAGACTATTAGGATCC-TTATTTTTCGAACTGCGGGTGGCTCCAGCCGCTGCCGTGCCCT-GGAAGTAAAGGTTTTCGAACAGACCCTTCTTTTCTTCTCTTCT-TGC-3'.

All primers for seamless cloning were Cloning Oligo (<60 bp) or EXTREmer (>60 bp) synthesis and purification quality from Eurofins Genomics, Germany. All restriction enzymes were FastDigest enzymes from Thermo Fisher Scientific. All plasmids were verified by sequencing (Eurofins Genomics, Germany) after each cloning step, including the midpreps used for protein production.

Production and purification of recombinant human and *Drosophila* septin complexes

pncS-vH and pncS plasmids were co-transformed into *E. coli* BL21(DE3), and co-transformants selected on LB agar plates with carbenicillin and spectinomycin each at 100 µg/ml. A single colony was selected to prepare an overnight preculture at 37°C with LB medium containing antibiotics at 100 µg/ml; the volume of the preculture was 1/50 of the final culture volume. Terrific broth with antibiotics at 50 µg/ml was inoculated with the pre-culture and incubated at 37°C. We typically prepared 3.5–5 l of culture: the culture volume per Erlenmeyer flask was 1/3 of the flask volume to allow for efficient oxygenation. For nonfluorescent septins, we let bacteria grow to $A_{600nm} \sim 2$ before inducing expression with 0.5 mM IPTG for 3 h at 37°C. For fluorescent septins, we let bacteria grow to $A_{600nm} \sim 0.6–0.8$ before inducing expression with 0.5 mM IPTG for overnight expression at 17°C; the incubator was protected from light with aluminum foil in this case. The culture was stopped by centrifuging at 3400 g for 15 min and 4°C, and the supernatant used to pool all bacteria pellets in 50-ml Falcon tubes, which were further centrifuged at 5000 g for 10 min and 4°C. Bacteria pellets were stored at –20°C until protein purification. Bacteria expressing GFP-tagged septins yield yellow-greenish pellets.

On the day of purification, we resuspended the pellet in ice-cold lysis buffer (50 mM Tris-HCl pH 8, 300 mM KCl, 5 mM MgCl₂, 0.25 mg/ml lysozyme, 1 mM PMSF, cOmplete™ protease inhibitor cocktail (1 tablet per 50 ml), 10 mg/l DNase I, 20 mM MgSO₄) using gentle agitation for 30 min at 4°C, and lysed cells on ice using a tip sonicator with 5 cycles of 30 s 'ON', 15 s 'OFF'. We typically use 100 ml of lysis buffer for a starting 3.5–5 L culture. The lysate was clarified by centrifugation for 30 min at 20,000 g and 4°C, the supernatant loaded on a StrepTrap HP column equilibrated with 50 mM Tris-HCl pH 8, 300 mM KCl, 5 mM MgCl₂ and the column washed with the same buffer. Strep-tag-II-containing septin complexes were eluted with 50 mM Tris-HCl pH 8, 300 mM KCl, 5 mM MgCl₂, and 2.5 mM desthiobiotin; desthiobiotin was prepared fresh right before use. All fractions contained in the elution peak were collected. The pooled fractions were then loaded to a HisTrap HP column equilibrated with 50 mM Tris-HCl pH 8, 300 mM KCl, 5 mM MgCl₂, the column washed with the same buffer, and His₆-tag-containing complexes eluted with 50 mM Tris-HCl at pH 8, 300 mM KCl, 5 mM MgCl₂, and 250 mM imidazole. We typically do not concentrate the protein further, thus we collect only the highest-concentration peak fractions (~0.6–1.2 ml). Both affinity column steps were performed on an ÄKTA pure protein purification system (Cytiva). To remove imidazole, we either performed an overnight dialysis step or used a PD-10 column, also including DTT in this last step. The final elution buffer, in which septins are stored, was 50 mM Tris-HCl

pH 8, 300 mM KCl, 5 mM MgCl₂ and 1 mM DTT. All purification steps were performed at 4°C. We typically purify septin complexes in a single day (starting from cell lysis) to minimize unnecessary exposure to proteases and contaminants and maintain protein integrity and functionality.

Protein concentrations were assessed with absorbance measurements at 280 nm using the calculated extinction coefficients for the respective complexes, and 20- or 50-μl aliquots were flash-frozen in liquid nitrogen and stored at -80°C until further use. This protocol typically yielded 0.5–1 ml of purified octamers at ~1–3 mg/ml (~2–6 μM) and 0.5–1 ml of purified hexamers at ~1–3 mg/ml (~3–9 μM) from a starting 3.5 l of bacterial culture. Extinction coefficients and molecular masses used for concentration conversions were computed from the primary amino acid sequences using ExPASy (<http://web.expasy.org/protparam/>) and considering two copies of each full-length septin, tags included, and are summarized in Table S1. The calculation of these parameters for mammalian and *Drosophila* hexamers were described in Mavrikakis et al. (2016).

Septin preparations were used closest to their purification and typically within 2–3 months upon storage at -80°C. Septin complexes were typically used within 3–4 days upon thawing and not frozen back. Electron microscopy of the purified septin complexes did not show significant aggregation necessitating a gel filtration step, thus the size exclusion chromatography step used previously (Mavrikakis et al., 2014, 2016) was not included. Purified protein was examined as such for EM, whereas it was systematically ultracentrifuged right before use for reconstitution assays using fluorescence microscopy to pellet any remaining or formed aggregates upon freezing (see respective methods below). We validated this purification protocol, and we have used it routinely in three different labs (at Institut Fresnel, Institut Curie and Delft University of Technology) with slight variations that do not affect the final result; for example, the order of StrepTrap HP and HisTrap HP columns can be inverted, or the nickel-affinity step can use batch resin instead of prepacked columns. This production and purification protocol was used to purify at least six preparations of human septin octamers-9_i1, six preparations of human septin octamers-9_i3, one preparation of human septin octamers-9_i5, and six preparations of human septin hexamers. The purification of mammalian septin octamers-9_i3, containing mouse SEPT2, human SEPT6, human SEPT7ΔN19, and human SEPT9_i3 (Fig. 2B, and left panel in Fig. 3B) was undertaken as described previously (Mavrikakis et al., 2014, 2016); the main difference with respect to the protocol described above is that the columns were inverted, nickel affinity used as a first step, and that we employed an additional gel filtration step.

Materials and reagents for septin complex production and purification

The sources and identifiers for the chemicals used for recombinant protein production and purification are as follows. *E. coli* BL21(DE3) competent cells from Agilent (200131) or Thermo Fisher Scientific (EC0114). Carbenicillin (for pNEA-vH selection) from Sigma (C3416), Condalab (6803) or Thermo Fisher Scientific (Fisher Bioreagents BP2648-1). Spectinomycin (for pNCs selection) from Sigma (S4014) or Thermo Fisher Scientific (Fisher Bioreagents BP2957-1). LB broth medium from Sigma (L3022) or Condalab (1231). LB agar from Sigma (L2897) or Condalab (1083). SOC medium from Sigma (S1797) or Thermo Fisher Scientific (Fisher Bioreagents BP9740). Terrific Broth from MP Biomedicals (091012017) or Thermo Fisher Scientific (Fisher Bioreagents BP2468-10). IPTG from Euromedex (EU0008-C). Imidazole with low absorbance at 280 nm from Fisher Scientific (Fisher Chemical I/0010/53). PMSF from Sigma (78830). Lysozyme from Euromedex (5933). cOmplete™ Protease Inhibitor Cocktail Tablets from Sigma (Roche, 11836145001). DNase I from Sigma (Roche, 10104159001). d-Desthiobiotin from Sigma (D1411). DTT from Sigma (D0632). HisTrap HP 1 ml columns from Cytiva (17524701). StrepTrap HP 1 ml columns from Cytiva (28907546). 20K MWCO Slide-A-Lyzer cassettes from Thermo Fisher Scientific (87735). PD-10 desalting columns from Cytiva (17085101).

SDS-PAGE and western blotting

We assessed septin preparation purity and protein integrity by SDS-PAGE and western blotting. Purified septin complexes were analyzed by SDS-PAGE using 4–20% precast polyacrylamide gels (Mini-PROTEAN TGX

Gels from Bio-Rad, 4561095), or hand-casted 12% or 15% Tris-glycine polyacrylamide gels, followed by staining with InstantBlue Coomassie stain (Expedeon, ISB1L) (Fig. S1C–E). Molecular mass markers were Precision Plus Protein All Blue Standards from Bio-Rad (1610373) in all gels shown apart from Fig. S1C (Pierce Unstained Protein MW Marker from Thermo Fisher Scientific, 26610) and Fig. S1D (PageRuler Plus Prestained Protein Ladder from Thermo Fisher Scientific, 26619). SDS-PAGE was performed for each septin preparation.

Western blots were performed for two different preparations for each nonfluorescent and SEPT2–msfGFP hexamer and two different preparations for each nonfluorescent and SEPT2–msfGFP long SEPT9 isoform-containing octamer, with similar results. Gels for western blot detection were loaded with 10 ng of purified protein. Gel, transfer membrane (Immobilon-P^{SO} membrane, Sigma ISE085R), filter pads and filter papers were incubated in transfer buffer (25 mM Tris, 192 mM glycine, 20% methanol) for 15 min before assembly in the Mini Trans-Blot transfer cell (Bio-Rad, 1703935). The transfer was done for 16 h at 4°C and at 110 mA constant current. The membrane was then blocked in a 5% (w/v) dry nonfat milk TBS-T solution [20 mM Tris-HCl pH 7.5, 200 mM NaCl and 0.1% (v/v) Tween20] for 2 h under constant agitation. Primary and secondary antibodies were diluted in the same blocking solution and incubated over the membrane for 60 min each under constant agitation. Between antibody incubations, membranes were washed three times for 10 min with TBS-T, the very last wash before detection only with TBS. To detect specific septins in recombinant human hexamers and octamers, we used rabbit anti-SEPT2 (1:2500, Sigma, HPA018481), rabbit anti-SEPT6 (1:1500, Santa Cruz Biotechnology, sc-20180), rabbit anti-SEPT7 (1:200, Santa Cruz Biotechnology, sc-20620), rabbit anti-SEPT9 (1:1500, Proteintech, 10769-1-AP), and HRP-conjugated anti-rabbit-IgG antibody (1:10,000, Cytiva, NA934). Chemiluminescent detection was undertaken with an Amersham ImageQuant 800 imager (Cytiva, 29399481) using Amersham ECL Select Western Blotting Detection Reagent (Cytiva, RPN2235) diluted five times in Milli-Q water. The membrane was incubated with the diluted reagent for 30 s, and washed for 10 s in TBS right before image acquisition. Images were collected in time series mode every 10 s, for a total of 50 images, and processed with ImageQuantTL software for molecular size calculation. In 4–20% Tris-glycine gels, the apparent mass of SEPT6 was larger than its calculated one by ~3 kDa, resulting in a band right above the one of SEPT7 that migrated as expected. The TEV-Strep-tag-II of SEPT7 in hexamer preparations adds 2.2 kDa to the SEPT7 band, which thus migrates much closer to SEPT6, making SEPT6 and SEPT7 bands hard to make out. All SEPT9 isoforms migrated much more slowly than their calculated masses; the apparent masses of the two long isoforms were larger by ~12–13 kDa, the one of the short isoform by ~5 kDa. Western blot analysis of hexamer and octamer preparations showed that all septins were intact, with the long N-terminal extension of SEPT9 being the most sensitive to proteolysis (Fig. S1F). The purity and protein integrity of septins in preparations, as well as the identification of protein bands in gels were corroborated by mass spectrometry analysis (see respective section below).

Given the sensitivity of the N-terminal extension of the long SEPT9 isoforms to proteolysis, we strongly recommend that western blots are systematically used to assess SEPT9 integrity, in particular when preparations are used for functional assays depending on isoform-specific sequences. Great care must be taken throughout lysis and purification to minimize contamination from proteases. N-terminal fusions of long SEPT9 isoforms can protect the N-terminal extensions from proteolysis (our data using msfGFP–SEPT9 fusions) and could be considered, as long as such fusions do not interfere with SEPT9 functionality. The presence of two copies of SEPT9 in the octamer cannot exclude that one copy has an intact N-terminus while the other copy has a partially degraded one, thus functional readouts remain the best way for assessing the integrity of the N-termini.

Mass spectrometry analysis and data processing

For analysis of septin hexamers and octamers (one preparation for each hexamer and for each long SEPT9 isoform-containing octamer), 1 μg of sample was loaded on 4–12% NuPAGE Novex Bis-Tris polyacrylamide gels (Thermo Scientific, NP0322BOX) and ran for 7 min at 80 V to stack

proteins in a single band. The gel was further stained with Imperial Protein Stain (Thermo Fisher Scientific, 24615), destained in water and proteins cut from the gel. Gel pieces (protein stack or cut protein bands) were subjected to in-gel trypsin digestion after cysteine reduction and alkylation (Shevchenko et al., 2006). Peptides were extracted from the gel and dried under vacuum. Samples were reconstituted with 0.1% trifluoroacetic acid in 2% acetonitrile and analyzed by liquid chromatography (LC)-tandem MS (MS/MS) using a Q Exactive Plus Hybrid Quadrupole-Orbitrap (Thermo Fisher Scientific, IQLAAEGAAPFALGMBDK) online with a nanoLC UltiMate 3000 chromatography system (Thermo Fisher Scientific, ULTIM3000RSLCNANO). 2 μ l corresponded to 10% of digested protein were injected in duplicate on the system. After pre-concentration and washing of the sample on a Acclaim PepMap 100 C18 column (2 cm \times 100 μ m i.d., 100 Å pore size, 5 μ m particle size, Thermo Fisher Scientific 164564-CMD), peptides were separated on a LC EASY-Spray C18 column (50 cm \times 75 μ m i.d., 100 Å pore size, 2 μ m particle size, Thermo Scientific ES803) at a flow rate of 300 nl/min with a two-step linear gradient (2–20% acetonitrile in 0.1% formic acid for 40 min and 20–40% acetonitrile in 0.1% formic acid for 10 min). For peptide ionization in the EASY-Spray source, spray voltage was set at 1.9 kV and the capillary temperature at 250°C. All samples were measured in a data-dependent acquisition mode. Each run was preceded by a blank MS run in order to monitor system background. The peptide masses were measured in a survey full scan [scan range 375–1500 m/z , with 70 K full width at half maximum (FWHM) resolution at m/z =400, target AGC value of 3.00×10^6 and maximum injection time of 100 ms]. Following the high-resolution full scan in the Orbitrap, the ten most intense data-dependent precursor ions were successively fragmented in the HCD cell and measured in Orbitrap (normalized collision energy of 27%, activation time of 10 ms, target AGC value of 1.00×10^5 , intensity threshold 1.00×10^4 maximum injection time 100 ms, isolation window 2 m/z , 17.5 K FWHM resolution, scan range 200 to 2000 m/z). Dynamic exclusion was implemented with a repeat count of 1 and exclusion duration of 10 s.

Raw files generated from mass spectrometry analysis were processed with Proteome Discoverer 1.4.1.14 (Thermo Fisher Scientific) to search against the proteome reference of the *Escherichia coli* protein database (4391 entries, extracted from Uniprot in August 2020). The original fasta file was populated with the sequences of the septin constructs contained in the measured preparations. Database search with Sequest HT was done using the following settings: a maximum of two missed trypsin cleavages allowed, methionine oxidation as a variable modification and cysteine carbamidomethylation as a fixed modification. A peptide mass tolerance of 10 ppm and a fragment mass tolerance of 0.6 Da were allowed for search analysis. Only peptides with high Sequest scores were selected for protein identification. The false discovery rate was set to 1% for protein identification.

To measure the relative protein abundance in septin preparations we employed the Top3 quantitation approach based on the correlation between the sum of the three most-intense peptide ions of a given protein and its absolute abundance (Silva et al., 2006). We divided the Top3 value of each identified protein in the protein stack by the sum of all Top3 values, generating a relative Top3 abundance measure, which correlates with the mol fraction of the protein. Septins constituted >97% of the total protein content, with the remaining <3% including GTP cyclohydrolase, biotin carboxylase and several chaperones (DnaK, DnaJ, GrpE and 60 kDa chaperonin). The results for molar fractions down to 0.02% are shown in Fig. S1G for a hexamer and two octamer preparations. The obtained mol fractions of septins, compared with the expected ones for hexamers (33%) and octamers (25%), point to the isolation of stoichiometric hexamers and octamers.

Tryptic peptides were used to identify and assign each septin to the detected bands by Coomassie staining, both for nonfluorescent and SEPT2–msfGFP hexamers and octamers, as shown in Fig. 1D and Fig. S1C–E, and septin band assignment was in line with the western blot analysis (Fig. S1F). Examples of tryptic peptide coverage for individual septins in recombinant hexamer, octamer-9_i1 and octamer-9_i3 preparations are shown in Fig. S1H, with coverages of 82% (SEPT2), 74% (SEPT6) and 70% (SEPT7) for hexamers, 82% (SEPT2), 70% (SEPT6), 69% (SEPT7) and 80% (SEPT9_i1) for octamers-9_i1, and 82% (SEPT2), 85% (SEPT6), 68%

(SEPT7) and 84% (SEPT9_i3) for octamers-9_i3. Tryptic peptides were identified throughout the sequence of each septin, including coiled-coils of all septins and the common N-terminal extension of the long SEPT9 isoforms, which together with the apparent band sizes from SDS-PAGE and the western blot analysis (Fig. 1D; Fig. S1F) supports that the isolated septin complexes are intact. Mass spectrometry of cut protein bands from native gels corresponding to 6mers, 8mers-9_i1 and 8mers-9_i3 (Fig. 1E) further confirmed the presence of intact, stoichiometric hexamers and octamers in the respective bands. Mass spectrometry of the cut protein band from native gels indicated by an asterisk in Fig. 1E, identified SEPT2, SEPT6, SEPT7, SEPT9 (in the case of octamers) and the chaperone DnaK in this band.

Coomassie-stained bands other than the annotated ones in our figures were identified as degradation products of septins or/and contaminants already identified in the analysis of the complexes from protein stacks. Degradation band analysis from different preparations suggested that the coiled-coils of SEPT2 and SEPT7 and the N-terminal extension of SEPT9 are most sensitive to proteolysis; the sensitivity of the latter to proteolysis was in line with results from western blots using antibodies against the C-terminal half of SEPT9 (Fig. S1F). The mass spectrometry proteomics data have been deposited to the ProteomeXchange Consortium via the PRIDE partner repository with the dataset identifier PXD023857.

Native PAGE

Native PAGE was performed on 4–16% NativePAGE Novex Bis-Tris polyacrylamide gels (Thermo Fisher Scientific, BN1002BOX) following instructions from the manufacturer. Briefly, 2 μ g of recombinant septin complexes, in their elution buffer (50 mM Tris-HCl pH 8, 300 mM KCl, 5 mM MgCl₂, 1 mM DTT), were diluted with water and 4 \times native PAGE sample buffer (Thermo Fisher Scientific, BN2003) to achieve a total KCl/NaCl concentration of ~100 mM and 1 \times native sample buffer, and were loaded in each gel well. Electrophoresis was performed at 150 V constant voltage until the migration front had reached one third of the gel, when dark cathode buffer was replaced with light anode buffer, then electrophoresis was pursued at 150 V until the migration front had reached the bottom of the gel. Gels were destained in 25% methanol and 10% acetic acid to eliminate most of the background (Coomassie stain from running buffer), then washed twice in pure water for 30 min, placed in Imperial Protein Stain (Thermo Fisher Scientific, 24615) for 1 h and destained in pure water overnight. Molecular mass standards were NativeMark Unstained Protein Standard (Thermo Fisher Scientific, LC0725). Native PAGE was performed for two independent preparations for human hexamers and for each long SEPT9 isoform-containing octamer, with similar results.

Hexamers migrated with an apparent size of ~310 kDa, which is in line with the calculated size (292 kDa). Octamers for both long SEPT9 isoform-containing octamers migrated with apparent sizes of ~600 kDa, and thus much more slowly than their theoretical sizes (423 kDa and 419 kDa, respectively), in line with reported gel filtration and density gradient centrifugation experiments showing that the long SEPT9 isoform-specific N-terminal extension confers a significant increase in the hydrodynamic radius slowing down octamer migration in native PAGE (Sellin et al., 2014).

Modeling of human septin octamers

Models of human septin octamers were generated in order to analyze and interpret the analytical ultracentrifugation sedimentation velocity experiments. A series of structures of the GTP-binding domains (GBDs) of SEPT2, 6, 7 and 9 have been solved by X-ray crystallography (Rosa et al., 2020; Valadares et al., 2017), with some flexible loops partially missing. The homology modelling software, SWISS-MODEL (Waterhouse et al., 2018), was used to complete the existing GBD structures. To search for templates, SWISS-MODEL uses BLAST (Camacho et al., 2009) and HHblits (Steinegger et al., 2019) for related evolutionary structures matching the target sequence within the SWISS-MODEL Template Library (SMTL version 2020-12-09, last included PDB release: 2020-12-04). For each identified template, the quality of the resulting model is predicted from features of the target–template alignment, and the template with the highest quality is selected for model building using ProMod3. Coordinates that are conserved between the target and the template are copied from the template to the model. Insertions and deletions are

remodeled using a fragment library. Finally, the geometry of the resulting model is regularized by using a CHARMM22/CMAP protein force field (Mackerell et al., 2004). The global and per-residue model quality is assessed using the QMEAN scoring function (Studer et al., 2020). GBD models, starting right after the end of the $\alpha 0$ helices and until the end of the $\alpha 6$ helices, were generated for SEPT2 37–306 (template PDB 6UPA), SEPT6 40–308 (template PDB 6UPR), SEPT7 48–316 (template PDB 6N0B), and SEPT9 295–568 (template PDB 5CYO; numbering based on SEPT9_i1). The lack of structural information for the short (~20–30-residue) N-terminal extensions of SEPT2, 6 and 7, including the $\alpha 0$ helices, prompted us not to model these regions. However, the long (~260–280-residue) N-terminal extension of the long SEPT9 isoforms, SEPT9_i1 and SEPT9_i3, is expected to have an important impact on the hydrodynamic properties of the complexes. The lack of structural information for this N-terminal extension, the absence of structural homologs for this region (as determined by using Phyre2 and SWISS-MODEL) and secondary structure predictions of disorder for this region (using Quick2D), prompted us to model the N-terminal extensions of SEPT9_i1 and SEPT9_i3 as random coils with Phyre 2 (Kelley et al., 2015), using an *ab initio* approach (Fig. S4A). The generated model of the N-terminal extension of SEPT9_i1 as a random coil was used to isolate the short (~30-residue) N-terminal extension of the short SEPT9 isoform, SEPT9_i5, for modeling the latter in SEPT9_i5-containing complexes (Fig. S4A). Structure prediction using RaptorX, an algorithm based on distance-based protein folding powered by deep learning (Xu, 2019), generated alternative models of the N-terminal extensions of SEPT9_i1 (Fig. S4D,E) and SEPT9_i3 (Fig. S4F), including an extended conformation of the N-terminal extension of SEPT9_i1 (Fig. S4D).

To account for the contribution of the predicted coiled-coils in the C-terminal extensions of SEPT2, 6 and 7 to the hydrodynamic properties of the complexes and thus their sedimentation behavior, we extended the GBD models to include the C-terminal domain from the end of the $\alpha 6$ helix onwards. Delineation of coiled-coil features was based on secondary structure prediction via Quick2D (Zimmermann et al., 2018). This tool integrates secondary structure predictions from different software, including coiled-coil prediction via MARCOIL (Delorenzi and Speed, 2002), PCOILS (Gruber et al., 2006) and COILS (Lupas et al., 1991). The consensus sequences assigned by all three coiled-coil prediction algorithms were used for modeling coiled-coil helices with CCFold software (Guzenko and Strelkov, 2018). The resulting coiled-coils encompass residues 310–349, 321–406 and 336–421 for SEPT2, 6 and 7, respectively.

The models built with SWISS-MODEL and CCFold were still missing the connections between the GBDs and coiled-coils for SEPT2, 6 and 7, the ends of the C-terminal domains right after the predicted CCs, and the C-terminal domain of SEPT9 after the $\alpha 6$ helix. Phyre2 (Kelley et al., 2015) was used to construct these flexible parts *ab initio* for SEPT2, 7 and 9; and by homology for the very end of SEPT6 as a structural homolog was found by the software. The different models were generated in the context of the full proteins for higher accuracy. The flexible parts linking the GBDs and coiled-coils and the remaining C-terminal features were isolated from the resulting models with PyMOL (open-source software; <https://pymol.org/>). GBDs, coiled-coils, flexible parts, the N-terminal extensions, and, when relevant, sfGFP (PDB 2B3P), were then combined with PyMOL. The connections between the GBDs and the coiled-coils for SEPT6 and 7 are of different length and thus were stretched out so that they cover the same distance between the GBDs and the start of the coiled-coils without any steric clashes and to allow for the aligning of coiled-coil helices of SEPT6 and 7. In the case of SEPT2, the three residues between the GBD and the coiled-coil were built directly with PyMOL.

Tetrameric SEPT2–SEPT6–SEPT7–SEPT9 and octameric SEPT2–SEPT6–SEPT7–SEPT9–SEPT9–SEPT7–SEPT6–SEPT2 complexes were built by fitting the modeled structures to the crystal structure of the SEPT2–SEPT6–SEPT7 trimer (PDB 2QAG) (Sirajuddin et al., 2007). The central SEPT9 NC interface dimer in the octamer was built by aligning the modeled monomer to the SEPT2 NC dimer of the filament present in the crystal packing of the SEPT2–SEPT6–SEPT7 trimer structure. The other subunits were subsequently assembled to the dimer SEPT9–SEPT9 by aligning the modeled monomers to the rest of the X-ray structure. The PDB files of the

modeled tetramers and octamers, with or without the C-terminal extensions, and with different orientations of the CC domains, were then used in HullRad to determine their diffusion coefficient and estimate their sedimentation coefficient using the full-length molecular mass of the respective complexes (see section on analytical ultracentrifugation below). The model with the extended conformation of the N-terminal extension of SEPT9_i1 (Fig. S4C) was used interchangeably for SEPT9_i3 for predicting the sedimentation behavior of such hypothetical complexes (Fig. S4B).

Analytical ultracentrifugation

A sedimentation velocity experiment was carried out for one preparation each of octamers-9_i1 (0.75 mg/ml), octamers-9_i3 (0.5 mg/ml), and SEPT2–msfGFP octamers-9_i5 (1.0 mg/ml) at 40,000 rpm and 20°C in a Beckman Optima XL-A analytical ultracentrifuge, using 12 mm double sector centerpieces in an AN-50 Ti rotor (Beckman Coulter). Scans were acquired in continuous mode at 280 nm, in the absorbance range of 0.1 to 1. The partial specific volume of the proteins and the density and viscosity of the buffer were calculated with SEDNTERP (Laue et al., 1992). At 20°C, the calculated partial specific volume for octamers-9_i1 and -9_i3 was 0.735 ml g^{−1} and for SEPT2–msfGFP octamers-9_i5 0.736 ml g^{−1}. The density and viscosity of the buffer (50 mM Tris-HCl pH 8, 300 mM KCl, 5 mM MgCl₂, 1 mM DTT or 1 mM TCEP) were 1.014 g ml^{−1} and 0.0102 poise, respectively. The data recorded from moving boundaries were analyzed in terms of continuous size distribution functions of sedimentation coefficient, *c*(*s*), using the program SEDFIT (Schuck and Rossmanith, 2000) and the apparent sedimentation coefficient at 20°C in water (*S*_{20,w}) determined by peak integration.

A short column sedimentation equilibrium experiment was carried out for one preparation each of SEPT2–msfGFP hexamers and SEPT2–msfGFP octamers-9_i5, at 11,000 rpm in a Beckman Optima XL-A analytical ultracentrifuge, using 60 µl of protein loading concentrations from 0.5 to 1.5 mg ml^{−1}, in a six-channel epon charcoal-filled centerpiece in an AN-50 Ti rotor (Beckman Coulter). Septins were in 50 mM Tris-HCl pH 8, 300 mM KCl, 5 mM MgCl₂, and 1 mM TCEP. Scans were acquired at appropriate wavelengths (280 nm and 485 nm) when sedimentation equilibrium was reached at 4°C. Average molecular masses were determined by fitting a sedimentation equilibrium model for a single sedimenting solute to individual data sets with SEDPHAT.

To determine the theoretical sedimentation coefficient, the PDB file of a given model (tetramer, hexamer or octamer, including GFP in the case of SEPT2–msfGFP complexes, with or without coiled-coils, and with coiled-coils in different orientations) was analyzed using HullRad (Fleming and Fleming, 2018) to determine the translational diffusion coefficient, *D*. The estimated sedimentation coefficient, *s*, was then obtained using the theoretical molecular mass, *M*, for each complex and the Svedberg equation below, with \bar{v} being the partial specific volume of the protein, ρ the solvent density, *R* the gas constant and *T* the temperature:

$$S = \frac{M(1 - \bar{v}\rho)D}{RT} \quad (1)$$

The theoretical sedimentation coefficients calculated in this manner are shown in Fig. 1G, Figs S11 and S4B.

Preparation of flow cells for fluorescence microscopy of *in vitro* reconstituted actin and septins

Microscope glass slides and coverslips were cleaned for 15 min in base-piranha solution (Milli-Q water, 30% ammonium hydroxide, 35% hydrogen peroxide at a 5:1:1 volume ratio), rinsed twice, 5 min each, with Milli-Q water in a bath sonicator, and stored in 0.1 M KOH up to 1 month. Right before assembling flow cells, slides and coverslips were rinsed twice, 5 min each time, with Milli-Q water and dried with synthetic air. Flow cells with ~10 µl channels were assembled by sandwiching ~2-mm-wide and ~2.5-cm-long strips of Parafilm between a cleaned glass slide and coverslip and melting on a hot plate at 120°C (Fig. 4B). The resulting chambers were passivated by incubating for 45 min with 1 M KOH, rinsing with actin polymerization buffer (see composition in the respective section), incubating for another 45 min with 0.2 mg/ml PLL-PEG, and rinsing with

actin polymerization buffer (5 mM Tris-HCl pH 8, 50 mM KCl, 1 mM MgCl_2 , 0.2 mM Na_2ATP and 1 mM DTT). Flow cells were placed in a Petri dish along with tissue paper soaked in water to prevent flow channels from drying during the incubation steps and until use.

The sources and identifiers for the materials and chemicals are as follows. Glass slides (26×76 mm; AA00000102E01FST20) and glass coverslips (24×60 mm; BB02400600A113FST0) were from Thermo Fisher Scientific. Ammonium hydroxide solution (221228) and hydrogen peroxide solution were from Sigma (95299). PLL-PEG was from SuSoS AG {PLL(20)-g[3.5]-PEG(2)}.

Sample preparation for fluorescence microscopy of *in vitro* reconstituted actin and septins

Lyophilized rabbit skeletal muscle G-actin was resuspended to 5 mg/ml (119 μM) in G-buffer (5 mM Tris-HCl pH 8, 0.2 mM Na_2ATP , 0.1 mM CaCl_2 , 1 mM DTT), aliquots snap-frozen in liquid nitrogen and stored at -80°C . Frozen aliquots were thawed and centrifuged for 30 min at 120,000 g in a benchtop Beckman air-driven ultracentrifuge (Beckman Coulter Airfuge, 340401) to clear the solution from aggregates. Clarified G-actin was kept at 4°C and used within 3–4 weeks.

For reconstitution experiments, G-actin was diluted with G-buffer to 5 μM , and polymerized at 1 μM final concentration in actin polymerization buffer (5 mM Tris-HCl pH 8, 50 mM KCl, 1 mM MgCl_2 , 0.2 mM Na_2ATP , 1 mM DTT), additionally containing 1 mM Trolox, 2 mM protocatechuic acid (PCA), 0.1 μM protocatechuate 3,4-dioxygenase (PCD) and 0.1% (w/v) methylcellulose. Trolox and the enzymatic oxygen scavenging system PCA-PCD were used to minimize photobleaching during fluorescence imaging (Cordes et al., 2009; Shi et al., 2010). Methylcellulose was used as a crowding agent to keep actin filaments close to the surface and facilitate their observation. To fluorescently label actin filaments, we polymerized G-actin in the presence of 1 μM Alexa Fluor 568-conjugated phalloidin.

For actin–septin reconstitution experiments, thawed septin aliquots were cleared for 15 min at 120,000 g in a Beckman airfuge right before use. To polymerize G-actin in the presence of septins, we followed the same procedure as above, but mixed G-actin with septins, either nonfluorescent ones or GFP-labeled septins (at a 20% GFP molar ratio for octamers-9_i1 and -9_i3, and 100% GFP for octamers-9_i5) to a final septin concentration of 0.3 μM , right before polymerization. Actin and actin–septin samples were prepared with a final volume of 10 μl , were loaded immediately into PLL-PEG-passivated flow channels upon mixing of the components to start polymerization, and flow channels were sealed with vasoline:lanoline:paraffin (VALAP; 1:1:1). The contributions of KCl and MgCl_2 from the septin elution buffer were taken into account to yield the same final composition of actin polymerization buffer. Actin and actin–septin samples were typically incubated overnight at room temperature in the dark before observation. Actin–septin assays were repeated at least four times, using at least two different preparations from each nonfluorescent and fluorescent hexamers, 8mers-9_i1 and 8mers-9_i3, and one preparation from fluorescent 8mers-9_i5, yielding similar results.

To polymerize septins in the absence of actin, we followed the same procedure as above, but replaced the G-actin solution with G-buffer. Septins were also polymerized in the absence of actin by overnight dialysis against a low-salt buffer (50 mM Tris-HCl pH 8, 50 mM KCl, 5 mM MgCl_2 , 1 mM DTT) at 4°C , then loaded into PLL-PEG-passivated flow channels in the presence of 1 mM Trolox, 2 mM PCA, 0.1 μM PCD and 0.1% (w/v) methylcellulose, and sealed as described above for observation. Septins were used at 20% or 100% GFP molar ratio, yielding similar results. Septin polymerization assays were repeated at least five times, using at least two different preparations from each nonfluorescent and fluorescent hexamers, 8mers-9_i1 and 8mers-9_i3, and one preparation from fluorescent 8mers-9_i5, yielding similar results.

Actin–septin samples with mammalian septin hexamers (Fig. S3C) were prepared as above with the difference that septins were nonfluorescent, and fluorescent actin was Alexa Fluor 488-conjugated G-actin (10% molar ratio) as described previously (Mavrikis et al., 2014, 2016). G-actin polymerization in this case occurred in the presence of nonfluorescent phalloidin.

The sources and identifiers for proteins, materials and chemicals are as follows. Rabbit skeletal muscle G-actin was from Cytoskeleton, Inc. (AKL99). Alexa Fluor 568–phalloidin was from Thermo Fisher Scientific (A12380). Nonfluorescent phalloidin (P2141), methylcellulose (M0512), Trolox (238813) and protocatechuic acid (03930590) were from Sigma. Protocatechuate 3,4-dioxygenase was from Sigma (P8279). 20K MWCO Slide-A-Lyzer MINI dialysis devices were from Thermo Fisher Scientific (69590).

Fluorescence microscope image acquisition and processing

Samples were imaged on an optical setup employing a confocal spinning disk unit (CSU-X1-M1 from Yokogawa) connected to the side-port of a Perfect Focus System-equipped inverted microscope (Eclipse Ti2-E from Nikon Instruments), using a Nikon Plan Apo $\times 100/1.45$ NA oil immersion objective lens, 488- and 561-nm Sapphire laser lines (Coherent) and an iXon Ultra 888 EMCCD camera (1024×1024 pixels, 13×13 μm pixel size, Andor, Oxford Instruments), resulting in an image pixel size of 65 nm. Images were acquired with an exposure time of 0.1 s. Time-lapse sequences were acquired with a time interval of 0.5 s for a duration of 15 s. Actin filaments and actin–septin bundles were imaged close to the surface. Septin filament bundles were also found at the surface, but the extensive clusters of interconnected human septin filament bundles were observed floating in the bulk of the flow channels. To capture such clusters, z -stacks were acquired over 10–50 μm using a Δz interval of 0.5 μm . The images shown correspond to octamers-9_i1 polymerized with 20% GFP-tagged septins (Fig. S2A), octamers-9_i3 polymerized with 100% GFP-tagged septins (Fig. S2B), octamers-9_i5 polymerized with 100% GFP-tagged septins (Fig. S2C), hexamers polymerized with 100% GFP-tagged septins (Fig. S2D), and *Drosophila* hexamers polymerized with 20% GFP-tagged septins (Fig. S2E). All examples shown depict polymerization upon dilution into low salt apart from Fig. S2D (left panel), which shows polymerization upon dialysis into low salt.

Images were processed with the open-source image processing software ImageJ/Fiji. Images of actin filaments and actin–septin bundles are from single planes. Images of septin filament bundles are from maximum-intensity z projections, except for *Drosophila* septins, for which single planes are shown given that their bundles are typically found primarily at the surface. The contrast of all images shown was adjusted post acquisition so that both dim and bright structures are visible. To saturate the signal in the actin bundles and make the weaker-intensity signal of single/thinner actin filaments visible, the contrast was enhanced on purpose (images labeled ‘contrast enhancement’ in Fig. 4C–E and Fig. S3A,B). All images shown use an inverted grayscale, with bright signals appearing black in a white background.

Actin–septin samples with mammalian septin hexamers (Fig. S3C) were imaged with a Nikon Apo TIRF $\times 100/1.49$ NA oil immersion objective lens mounted on an Eclipse Ti microscope (Nikon Instruments) using a 491 nm laser line and imaged with a QuantEM 512SC EMCCD camera (Photometrics). Images were acquired with an exposure time of 0.1 s.

Transmission electron microscopy

Negative stain electron microscopy

Samples (4 μl) at final septin concentrations of 0.01–0.02 mg/ml (~ 25 –50 nM) for high-salt conditions (50 mM Tris-HCl pH 8, 300 mM KCl, 2 mM MgCl_2) or 0.05–0.1 mg/ml (~ 125 –250 nM) for low-salt conditions (50 mM Tris-HCl pH 8, 50 mM KCl, 2 mM MgCl_2) were adsorbed for 30 s (for high-salt conditions) to 1 h in a humid chamber (for low-salt conditions) on a glow-discharged carbon-coated grid (Electron Microscopy Sciences, CF300-CU). For low-salt conditions, septins were polymerized by dilution into low-salt buffer and incubated for 1 h to overnight at room temperature before grid adsorption. In the case of GFP-labeled septins, septins were polymerized without mixing with nonfluorescent ones. The grids were rinsed and negatively stained for 1 min using 1% (w/v) uranyl formate. Images for the qualitative examination of the morphology of septin assemblies were collected using a Tecnai Spirit microscope (Thermo Fisher Scientific, FEI) operated at an acceleration voltage of 80 kV and equipped with a Quemesa camera (Olympus). In addition to the EM experiments described above, which were performed at Institut Curie, EM was also performed at TU Delft following a

similar protocol. Septins were polymerized by dilution into a low-salt buffer (25 mM Tris-HCl pH 7.4, 50 mM KCl, 2.5 mM MgCl₂, 1 mM DTT) at a final septin concentration of 1 μ M for 1 h. The solution was then adsorbed to a glow discharged grid for 1 min, rinsed, negatively stained with 2% (w/v) uranyl acetate for 30 s and air dried. Images were collected with a JEM-1400plus TEM microscope (JEOL) operated at 120 kV equipped with 4k \times 4k F416 CMOS camera (TVIPS). Septin filament bundle length and width measurements (Fig. S2H) were made with the line tool in ImageJ/Fiji, and boxplots generated in Matlab. The narrow interfilament spacing (\sim 5 nm) in paired filaments mentioned in the main text refers to center-to-center spacing, and was deduced from paired filament width measurements assuming a monomer size of \sim 3.5 nm. Electron microscopy was performed with at least two different preparations from each nonfluorescent and fluorescent hexamers, 8mers-9_i1, 8mers-9_i3 and 8mers-9_i5. The images shown correspond to nonfluorescent octamers-9_i1 (Fig. 3Ai,ii), octamers-9_i3 (Fig. 3B) and octamers-9_i5 (Fig. 3C), SEPT2–msfGFP octamers-9_i1 (Fig. 3Aiii–v), SEPT2–msfGFP hexamers (Fig. S2F) and nonfluorescent mammalian hexamers (Fig. S2G).

Two-dimensional image processing for single-particle EM images

Images for single-particle analysis were collected using a Lab6 G2 Tecnai microscope (Thermo Fisher Scientific) operated at an acceleration voltage of 200 kV. Images were acquired with a 4k \times 4k F416 CMOS camera (TVIPS) in an automated manner using the EMTools software suite (TVIPS) with a pixel size of 2.13 Å and an electron dose of \sim 15 electrons/Å². 2D processing was carried out on septin rods incubated in high-salt conditions (50 mM Tris-HCl pH 8, 300 mM KCl, 2 mM MgCl₂) to determine the integrity of the complexes and pinpoint the arrangement of septin subunits within the complex. About 100 images were collected for each septin complex for image processing. Individual particles (septin rods) were hand-picked from the images using the boxer tool from the EMAN software suite (Ludtke et al., 1999). About 20–30 particles (203 \times 203 pixel boxes) were extracted per image. Subsequent processing was carried out using SPIDER (Frank et al., 1996). After normalization of the particles, a non-biased reference-free algorithm was used to generate 20 classes. Those classes were further used as references to pursue 2D multivariate statistical analysis. Multi-reference alignment followed by hierarchical classification involving principal component analysis was thereafter carried out to generate classes containing 50–100 particles. Each of the classes are representative of specific features within a given sample. This processing enabled us to quantify the distribution of particles in each dataset regarding the dimension of the rods as well as the presence of an additional electron density (GFP tag). For mammalian octamers-9_i3 (Fig. 2B), 4000 particles were selected with a distribution of 50% octamers, 23.7% heptamers, 23.5% hexamers, 1.4% pentamers and 1.4% tetramers. For human SEPT2–msfGFP octamers-9_i1 (Fig. 2C), 3266 particles were picked with a distribution of 57.9% octamers, 32.1% heptamers and 10.1% hexamers. An additional density towards the ends of the rods was pinpointed for 46.2% of the particles. For human SEPT2–msfGFP hexamers (Fig. 2D), 2976 particles were selected with a distribution of 97.7% hexamers and 2.3% pentamers. An additional density towards the ends of the rods could be pinpointed for 53.6% of the particles.

Acknowledgements

We thank Josette Perrier and Cendrine Nicoletti (iSm2, Marseille, France) for generously hosting protein production and purification experiments; Christophe Romier (IGBMC, Strasbourg, France) and Jean-Denis Pedelacq (IPBS, Toulouse, France) for advice on protein purification; Jeffrey den Haan (TU Delft, The Netherlands) for help with protein purification; Cristel Chandre (I2M, Marseille, France) for help with Matlab code; Caio Vaz Rimoli, Louwrens van Dellen and Sophie Brasselet (Institut Fresnel, Marseille, France) for the development of the spinning disk optical setup and image acquisition software. Proteomic analyses were done using the mass spectrometry facility of Marseille Proteomics (marseille-proteomique.univ-amu.fr) supported by IBISA (Infrastructures Biologie Santé et Agronomie), Plateforme Technologique Aix-Marseille, the Cancéropôle PACA, the Provence-Alpes-Côte d'Azur Région, the Institut Paoli-Calmettes and the Centre de Recherche en Cancérologie de Marseille, the Fonds Européen de Développement Régional and Plan Cancer. We further acknowledge the Cell and Tissue Imaging platform (PICT IBISA, Institut Curie) supported by France-Biolmaging (ANR-10-INBS-04).

Competing interests

The authors declare no competing or financial interests.

Author contributions

Conceptualization: G.H.K., A.B., M.M.; Methodology: M.M.; Investigation: F.I., C.S.M., G.C.-L., C.T., P.B., P.V.-P., L.C., S.A., F.-C.T., L.R., A.L., M.B., K.N., A.D.C., A.B., M.M.; Resources: R.V.; Writing - original draft: M.M.; Writing - review & editing: C.S.M., G.C.-L., C.T., P.B., P.V.-P., L.C., S.A., F.-C.T., J.W., S.C., G.H.K., A.B., M.M.; Supervision: R.V., J.W., S.C., G.H.K., A.B., M.M.; Project administration: M.M.; Funding acquisition: J.W., G.H.K., M.M.

Funding

This research received funding from the Agence Nationale de la Recherche (ANR grant ANR-17-CE13-0014; SEPTIMORF), the Fondation ARC pour la recherche sur le cancer (grant PJA 20151203182), the Fondation pour la Recherche Médicale (FRM grant ING20150531962) and the Cancéropôle PACA and INCa. This project has received funding from the European Research Council (ERC) under the European Union's Horizon 2020 research and innovation programme (grant agreement No 723241). This work was further financially supported by the Netherlands Organization for Scientific Research (Nederlandse Organisatie voor Wetenschappelijk Onderzoek, NWO/OCW) through a VIDI grant (project number: 680-47-233) and the 'BaSyC–Building a Synthetic Cell' Gravitation grant (024.003.019), and from the French Ministry of Foreign Affairs (Ministère des Affaires Étrangères), the French Ministry of Higher Education and Research (Ministère de l'Enseignement supérieur et de la Recherche) and the Dutch Ministry of Education, Culture and Science (Ministerie van Onderwijs, Cultuur en Wetenschap) through the Franco–Dutch Hubert–Curien partnership (PHC Van Gogh grants 25005UA and 28879SJ).

Data availability

The mass spectrometry proteomics data have been deposited to the ProteomeXchange Consortium via the PRIDE partner repository with the dataset identifier PXD023857.

References

- Akhmetova, K., Balasov, M., Huijbregts, R. P. and Chesnokov, I. (2015). Functional insight into the role of Orc6 in septin complex filament formation in *Drosophila*. *Mol. Biol. Cell* **26**, 15–28. doi:10.1091/mbc.e14-02-0734
- Akil, A., Peng, J., Omrane, M., Gondeau, C., Desterke, C., Marin, M., Tronchere, H., Tavenau, C., Sar, S., Briolotti, P. et al. (2016). Septin 9 induces lipid droplets growth by a phosphatidylinositol-5-phosphate and microtubule-dependent mechanism hijacked by HCV. *Nat. Commun.* **7**, 12203. doi:10.1038/ncomms12203
- Bai, X., Bowen, J. R., Knox, T. K., Zhou, K., Pendziwiat, M., Kuhlensbaumer, G., Sindelar, C. V. and Spiliotis, E. T. (2013). Novel septin 9 repeat motifs altered in neurogenic amyotrophy bind and bundle microtubules. *J. Cell Biol.* **203**, 895–905. doi:10.1083/jcb.201308068
- Bertin, A., McMurray, M. A., Grob, P., Park, S. S., Garcia, G., III, Patanwala, I., Ng, H. L., Alber, T., Thorner, J. and Nogales, E. (2008). Saccharomyces cerevisiae septins: supramolecular organization of heterooligomers and the mechanism of filament assembly. *Proc. Natl. Acad. Sci. USA* **105**, 8274–8279. doi:10.1073/pnas.0803301105
- Bertin, A., McMurray, M. A., Thai, L., Garcia, G., III, Votin, V., Grob, P., Allyn, T., Thorner, J. and Nogales, E. (2010). Phosphatidylinositol-4,5-bisphosphate promotes budding yeast septin filament assembly and organization. *J. Mol. Biol.* **404**, 711–731. doi:10.1016/j.jmb.2010.10.002
- Bertin, A., McMurray, M. A., Pierson, J., Thai, L., McDonald, K. L., Zehr, E. A., Garcia, G., III, Peters, P., Thorner, J. and Nogales, E. (2012). Three-dimensional ultrastructure of the septin filament network in *Saccharomyces cerevisiae*. *Mol. Biol. Cell* **23**, 423–432. doi:10.1091/mbc.e11-10-0850
- Bowen, J. R., Hwang, D., Bai, X., Roy, D. and Spiliotis, E. T. (2011). Septin GTPases spatially guide microtubule organization and plus end dynamics in polarizing epithelia. *J. Cell Biol.* **194**, 187–197. doi:10.1083/jcb.201102076
- Bridges, A. A., Zhang, H., Mehta, S. B., Occhipinti, P., Tani, T. and Gladfelter, A. S. (2014). Septin assemblies form by diffusion-driven annealing on membranes. *Proc. Natl. Acad. Sci. USA* **111**, 2146–2151. doi:10.1073/pnas.1314138111
- Bridges, A. A., Jentsch, M. S., Oakes, P. W., Occhipinti, P. and Gladfelter, A. S. (2016). Micron-scale plasma membrane curvature is recognized by the septin cytoskeleton. *J. Cell Biol.* **213**, 23–32. doi:10.1083/jcb.201512029
- Burrows, J. F., Chanduloy, S., McIlhatton, M. A., Nagar, H., Yeates, K., Donaghy, P., Price, J., Godwin, A. K., Johnston, P. G. and Russell, S. E. (2003). Altered expression of the septin gene, SEPT9, in ovarian neoplasia. *J. Pathol.* **201**, 581–588. doi:10.1002/path.1484
- Byers, B. and Goetsch, L. (1976). A highly ordered ring of membrane-associated filaments in budding yeast. *J. Cell Biol.* **69**, 717–721. doi:10.1083/jcb.69.3.717

- Calvo, F., Ranftl, R., Hooper, S., Farrugia, A. J., Moeendarbary, E., Bruckbauer, A., Batista, F., Charras, G. and Sahai, E. (2015). Cdc42EP3/BORG2 and septin network enables mechano-transduction and the emergence of cancer-associated fibroblasts. *Cell Rep* **13**, 2699-2714. doi:10.1016/j.celrep.2015.11.052
- Camacho, C., Coulouris, G., Avagyan, V., Ma, N., Papadopoulos, J., Bealer, K. and Madden, T. L. (2009). BLAST+: architecture and applications. *BMC Bioinformatics* **10**, 421. doi:10.1186/1471-2105-10-421
- Cao, L., Ding, X., Yu, W., Yang, X., Shen, S. and Yu, L. (2007). Phylogenetic and evolutionary analysis of the septin protein family in metazoan. *FEBS Lett* **581**, 5526-5532. doi:10.1016/j.febslet.2007.10.032
- Casamayor, A. and Snyder, M. (2003). Molecular dissection of a yeast septin: distinct domains are required for septin interaction, localization, and function. *Mol. Cell Biol.* **23**, 2762-2777. doi:10.1128/MCB.23.8.2762-2777.2003
- Castro, D., da Silva, S. M. O., Pereira, H. D., Macedo, J. N. A., Leonardo, D. A., Valadares, N. F., Kumagai, P. S., Brandao-Neto, J., Araujo, A. P. U. and Garratt, R. C. (2020). A complete compendium of crystal structures for the human SEPT3 subgroup reveals functional plasticity at a specific septin interface. *IUCrJ* **7**, 462-479. doi:10.1107/S2052252520002973
- Collie, A. M., Landsverk, M. L., Ruzzo, E., Mefford, H. C., Buysse, K., Adkins, J. R., Knutzen, D. M., Barnett, K., Brown, R. H., Jr, Parry, G. J. et al. (2010). Non-recurrent SEPT9 duplications cause hereditary neuralgic amyotrophy. *J. Med. Genet.* **47**, 601-607. doi:10.1136/jmg.2009.072348
- Connolly, D., Hoang, H. G., Adler, E., Tazearslan, C., Simmons, N., Bernard, V. V., Castaldi, M., Oktay, M. H. and Montagna, C. (2014). Septin 9 amplification and isoform-specific expression in peritumoral and tumor breast tissue. *Biol. Chem.* **395**, 157-167. doi:10.1515/hsz-2013-0247
- Connolly, D., Yang, Z., Castaldi, M., Simmons, N., Oktay, M. H., Coniglio, S., Fazzari, M. J., Verdier-Pinard, P. and Montagna, C. (2011). Septin 9 isoform expression, localization and epigenetic changes during human and mouse breast cancer progression. *Breast Cancer Res.* **13**, R76. doi:10.1186/bcr2924
- Cordes, T., Vogelsang, J. and Tinnefeld, P. (2009). On the mechanism of Trolox as antiblinking and antibleaching reagent. *J. Am. Chem. Soc.* **131**, 5018-5019. doi:10.1021/ja809117z
- Costantini, L. M., Fossati, M., Francolini, M. and Snapp, E. L. (2012). Assessing the tendency of fluorescent proteins to oligomerize under physiologic conditions. *Traffic* **13**, 643-649. doi:10.1111/j.1600-0854.2012.01336.x
- Cranfill, P. J., Sell, B. R., Baird, M. A., Allen, J. R., Lavagnino, Z., de Gruiter, H. M., Kremers, G. J., Davidson, M. W., Ustione, A. and Piston, D. W. (2016). Quantitative assessment of fluorescent proteins. *Nat. Methods* **13**, 557-562. doi:10.1038/nmeth.3891
- Damalia, J. C., Nobre, T. M., Lopes, J. L., Oliveira, O. N., Jr and Araujo, A. P. (2013). Lipid interaction triggering Septin2 to assemble into beta-sheet structures investigated by Langmuir monolayers and PM-IRRAS. *Biochim. Biophys. Acta* **1828**, 1441-1448. doi:10.1016/j.bbame.2013.02.003
- de Almeida Marques, I., Valadares, N. F., Garcia, W., Damalia, J. C., Macedo, J. N., de Araujo, A. P., Botello, C. A., Andreu, J. M. and Garratt, R. C. (2012). Septin C-terminal domain interactions: implications for filament stability and assembly. *Cell Biochem. Biophys.* **62**, 317-328. doi:10.1007/s12013-011-9307-0
- Delorenzi, M. and Speed, T. (2002). An HMM model for coiled-coil domains and a comparison with PSSM-based predictions. *Bioinformatics* **18**, 617-625. doi:10.1093/bioinformatics/18.4.617
- DeRose, B. T., Kelley, R. S., Ravi, R., Kokona, B., Beld, J., Spiliotis, E. T. and Padrick, S. B. (2020). Production and analysis of a mammalian septin hetero-octamer complex. *Cytoskeleton (Hoboken)* **77**, 485-499. doi:10.1002/cm.21643
- Diebold, M. L., Fribourg, S., Koch, M., Metzger, T. and Romier, C. (2011). Deciphering correct strategies for multiprotein complex assembly by co-expression: application to complexes as large as the histone octamer. *J. Struct. Biol.* **175**, 178-188. doi:10.1016/j.jsb.2011.02.001
- Dolat, L., Hu, Q. and Spiliotis, E. T. (2014a). Septin functions in organ system physiology and pathology. *Biol. Chem.* **395**, 123-141. doi:10.1515/hsz-2013-0233
- Dolat, L., Hunyara, J. L., Bowen, J. R., Karasmanis, E. P., Elgawly, M., Galkin, V. E. and Spiliotis, E. T. (2014b). Septins promote stress fiber-mediated maturation of focal adhesions and renal epithelial motility. *J. Cell Biol.* **207**, 225-235. doi:10.1083/jcb.201405050
- Dolat, L. and Spiliotis, E. T. (2016). Septins promote macropinosome maturation and traffic to the lysosome by facilitating membrane fusion. *J. Cell Biol.* **214**, 517-527. doi:10.1083/jcb.201603030
- Estey, M. P., Di Ciano-Oliveira, C., Froese, C. D., Bejide, M. T. and Trimble, W. S. (2010). Distinct roles of septins in cytokinesis: SEPT9 mediates midbody abscission. *J. Cell Biol.* **191**, 741-749. doi:10.1083/jcb.201006031
- Estey, M. P., Di Ciano-Oliveira, C., Froese, C. D., Fung, K. Y. Y., Steels, J. D., Litchfield, D. W. and Trimble, W. S. (2013). Mitotic regulation of SEPT9 protein by cyclin-dependent kinase 1 (Cdk1) and Pin1 protein is important for the completion of cytokinesis. *J. Biol. Chem.* **288**, 30075-30086. doi:10.1074/jbc.M113.474932
- Farkasovsky, M., Herter, P., Voss, B. and Wittinghofer, A. (2005). Nucleotide binding and filament assembly of recombinant yeast septin complexes. *Biol. Chem.* **386**, 643-656. doi:10.1515/BC.2005.075
- Field, C. M., al-Awar, O., Rosenblatt, J., Wong, M. L., Alberts, B. and Mitchison, T. J. (1996). A purified *Drosophila* septin complex forms filaments and exhibits GTPase activity. *J. Cell Biol.* **133**, 605-616. doi:10.1083/jcb.133.3.605
- Fleming, P. J. and Fleming, K. G. (2018). HULLRAD: Fast Calculations of Folded and Disordered Protein and Nucleic Acid Hydrodynamic Properties. *Biophys. J.* **114**, 856-869. doi:10.1016/j.bpj.2018.01.002
- Frank, J., Radermacher, M., Penczek, P., Zhu, J., Li, Y., Ladjadj, M. and Leith, A. (1996). SPIDER and WEB: processing and visualization of images in 3D electron microscopy and related fields. *J. Struct. Biol.* **116**, 190-199. doi:10.1006/jsbi.1996.0030
- Frazier, J. A., Wong, M. L., Longtine, M. S., Pringle, J. R., Mann, M., Mitchison, T. J. and Field, C. (1998). Polymerization of purified yeast septins: evidence that organized filament arrays may not be required for septin function. *J. Cell Biol.* **143**, 737-749. doi:10.1083/jcb.143.3.737
- Fuchtbauer, A., Lassen, L. B., Jensen, A. B., Howard, J., Quiroga Ade, S., Warming, S., Sorensen, A. B., Pedersen, F. S. and Fuchtbauer, E. M. (2011). Septin9 is involved in septin filament formation and cellular stability. *Biol. Chem.* **392**, 769-777. doi:10.1515/BC.2011.088
- Fung, K. Y., Dai, L. and Trimble, W. S. (2014). Cell and molecular biology of septins. *Int. Rev. Cell Mol. Biol.* **310**, 289-339. doi:10.1016/B978-0-12-800180-6.00007-4
- Garcia, W., de Araujo, A. P., Neto Mde, O., Ballester, M. R., Polikarpov, I., Tanaka, M., Tanaka, T. and Garratt, R. C. (2006). Dissection of a human septin: definition and characterization of distinct domains within human SEPT4. *Biochemistry* **45**, 13918-13931. doi:10.1021/bi061549z
- Garcia, G., Ill, Bertin, A., Li, Z., Song, Y., McMurray, M. A., Thorner, J. and Nogales, E. (2011). Subunit-dependent modulation of septin assembly: budding yeast septin Shs1 promotes ring and gauze formation. *J. Cell Biol.* **195**, 993-1004. doi:10.1083/jcb.201107123
- Gruber, M., Soding, J. and Lupas, A. N. (2006). Comparative analysis of coiled-coil prediction methods. *J. Struct. Biol.* **155**, 140-145. doi:10.1016/j.jsb.2006.03.009
- Guzenko, D. and Strelkov, S. V. (2018). CCFold: rapid and accurate prediction of coiled-coil structures and application to modelling intermediate filaments. *Bioinformatics* **34**, 215-222. doi:10.1093/bioinformatics/btx551
- Hall, P. A., Jung, K., Hillan, K. J. and Russell, S. E. (2005). Expression profiling the human septin gene family. *J. Pathol.* **206**, 269-278. doi:10.1002/path.1789
- Hall, P. A., Bruford, E., Russell, S. E. H., Macara, I. G. and Pringle, J. R. (2008). Mammalian septin nomenclature. In *The Septins* (ed. P.A. Hall, S.E.H. Russell and J.R. Pringle), pp. 351-354. John Wiley & Sons, Ltd.
- Hannibal, M. C., Ruzzo, E. K., Miller, L. R., Betz, B., Buchan, J. G., Knutzen, D. M., Barnett, K., Landsverk, M. L., Brice, A., LeGuern, E. et al. (2009). SEPT9 gene sequencing analysis reveals recurrent mutations in hereditary neuralgic amyotrophy. *Neurology* **72**, 1755-1759. doi:10.1212/WNL.0b013e3181a609e3
- Hartwell, L. H. (1971). Genetic control of the cell division cycle in yeast. IV. Genes controlling bud emergence and cytokinesis. *Exp. Cell Res.* **69**, 265-276. doi:10.1016/0014-4827(71)90223-0
- Hartwell, L. H., Culotti, J. and Reid, B. (1970). Genetic control of the cell-division cycle in yeast. I. Detection of mutants. *Proc. Natl. Acad. Sci. USA* **66**, 352-359. doi:10.1073/pnas.66.2.352
- Hsu, S. C., Hazuka, C. D., Roth, R., Foletti, D. L., Heuser, J. and Scheller, R. H. (1998). Subunit composition, protein interactions, and structures of the mammalian brain sec6/8 complex and septin filaments. *Neuron* **20**, 1111-1122. doi:10.1016/S0896-6273(00)80493-6
- Huijbregts, R. P., Svitin, A., Stinnett, M. W., Renfrow, M. B. and Chesnokov, I. (2009). *Drosophila* Orc6 facilitates GTPase activity and filament formation of the septin complex. *Mol. Biol. Cell* **20**, 270-281. doi:10.1091/mbc.e08-07-0754
- John, C. M., Hite, R. K., Weirich, C. S., Fitzgerald, D. J., Jawhari, H., Faty, M., Schlappfer, D., Kroschewski, R., Winkler, F. K., Walz, T. et al. (2007). The *Caenorhabditis elegans* septin complex is nonpolar. *EMBO J.* **26**, 3296-3307. doi:10.1038/sj.emboj.7601775
- Joo, E., Surka, M. C. and Trimble, W. S. (2007). Mammalian SEPT2 is required for scaffolding nonmuscle myosin II and its kinases. *Dev. Cell* **13**, 677-690. doi:10.1016/j.devcel.2007.09.001
- Kelley, L. A., Mezulis, S., Yates, C. M., Wass, M. N. and Sternberg, M. J. (2015). The PyMol web portal for protein modeling, prediction and analysis. *Nat. Protoc.* **10**, 845-858. doi:10.1038/nprot.2015.053
- Kim, M. S., Froese, C. D., Estey, M. P. and Trimble, W. S. (2011). SEPT9 occupies the terminal positions in septin octamers and mediates polymerization-dependent functions in abscission. *J. Cell Biol.* **195**, 815-826. doi:10.1083/jcb.201106131
- Kim, M. S., Froese, C. D., Xie, H. and Trimble, W. S. (2012). Uncovering principles that control septin-septin interactions. *J. Biol. Chem.* **287**, 30406-30413. doi:10.1074/jbc.M112.387464
- Kinoshita, M. (2003). Assembly of mammalian septins. *J. Biochem.* **134**, 491-496. doi:10.1093/jb/mvg182
- Kinoshita, M., Kumar, S., Mizoguchi, A., Ide, C., Kinoshita, A., Haraguchi, T., Hiraoka, Y. and Noda, M. (1997). Nedd5, a mammalian septin, is a novel cytoskeletal component interacting with actin-based structures. *Genes Dev.* **11**, 1535-1547. doi:10.1101/gad.11.12.1535

- Kinoshita, M., Field, C. M., Coughlin, M. L., Straight, A. F. and Mitchison, T. J. (2002). Self- and actin-templated assembly of Mammalian septins. *Dev. Cell* **3**, 791-802. doi:10.1016/S1534-5807(02)00366-0
- Kuhlenbaumer, G., Hannibal, M. C., Nelis, E., Schirmacher, A., Verpoorten, N., Meuleman, J., Watts, G. D., De Vriendt, E., Young, P., Stogbauer, F. et al. (2005). Mutations in SEPT9 cause hereditary neuralgic amyotrophy. *Nat. Genet.* **37**, 1044-1046. doi:10.1038/ng1649
- Kumagai, P. S., Martins, C. S., Sales, E. M., Rosa, H. V. D., Mendonca, D. C., Damalio, J. C. P., Spinozzi, F., Itri, R. and Araujo, A. P. U. (2019). Correct partner makes the difference: Septin G-interface plays a critical role in amyloid formation. *Int. J. Biol. Macromol.* **133**, 428-435. doi:10.1016/j.ijbiomac.2019.04.105
- Landsverk, M. L., Ruzzo, E. K., Mefford, H. C., Buysse, K., Buchan, J. G., Eichler, E. E., Petty, E. M., Peterson, E. A., Knutzen, D. M., Barnett, K. et al. (2009). Duplication within the SEPT9 gene associated with a founder effect in North American families with hereditary neuralgic amyotrophy. *Hum. Mol. Genet.* **18**, 1200-1208. doi:10.1093/hmg/ddp014
- Laue, T. M., Shah, B., Ridgeway, T. M. and Pelletier, S. L. (1992). Computer-aided interpretation of analytical sedimentation data for proteins. In *Analytical Ultracentrifugation in Biochemistry and Polymer Science* (ed. S.E. Harding, J.C. Horton and A.J. Rowe), pp. 90-125. Royal Society of Chemistry.
- Leonardo, D. A., Cavini, I. A., Sala, F. A., Mendonca, D. C., Rosa, H. V. D., Kumagai, P. S., Crusca, E., Jr, Valadares, N. F., Marques, I. A., Brandao-Neto, J. et al. (2021). Orientational ambiguity in septin coiled coils and its structural basis. *J. Mol. Biol.* **433**, 166889. doi:10.1016/j.jmb.2021.166889
- Liu, Z., Vong, Q. P., Liu, C. and Zheng, Y. (2014). Borg5 is required for angiogenesis by regulating persistent directional migration of the cardiac microvascular endothelial cells. *Mol. Biol. Cell* **25**, 841-851. doi:10.1091/mbc.e13-09-0543
- Low, C. and Macara, I. G. (2006). Structural analysis of septin 2, 6, and 7 complexes. *J. Biol. Chem.* **281**, 30697-30706. doi:10.1074/jbc.M605179200
- Ludtke, S. J., Baldwin, P. R. and Chiu, W. (1999). EMAN: semiautomated software for high-resolution single-particle reconstructions. *J. Struct. Biol.* **128**, 82-97. doi:10.1006/j.sbi.1999.4174
- Lupas, A., Van Dyke, M. and Stock, J. (1991). Predicting coiled coils from protein sequences. *Science* **252**, 1162-1164. doi:10.1126/science.252.5009.1162
- Macara, I. G., Baldarelli, R., Field, C. M., Glotzer, M., Hayashi, Y., Hsu, S. C., Kennedy, M. B., Kinoshita, M., Longtine, M., Low, C. et al. (2002). Mammalian septins nomenclature. *Mol. Biol. Cell* **13**, 4111-4113. doi:10.1091/mbc.e02-07-0438
- Mackerell, A. D., Jr, Feig, M. and Brooks, C. L.III (2004). Extending the treatment of backbone energetics in protein force fields: limitations of gas-phase quantum mechanics in reproducing protein conformational distributions in molecular dynamics simulations. *J. Comput. Chem.* **25**, 1400-1415. doi:10.1002/jcc.20065
- Marquardt, J., Chen, X. and Bi, E. (2019). Architecture, remodeling, and functions of the septin cytoskeleton. *Cytoskeleton (Hoboken)* **76**, 7-14. doi:10.1002/cm.21475
- Mavrikakis, M., Azou-Gros, Y., Tsai, F. C., Alvarado, J., Bertin, A., Iv, F., Kress, A., Brasselet, S., Koenderink, G. H. and Lecuit, T. (2014). Septins promote F-actin ring formation by crosslinking actin filaments into curved bundles. *Nat. Cell Biol.* **16**, 322-334. doi:10.1038/ncb2921
- Mavrikakis, M., Tsai, F. C. and Koenderink, G. H. (2016). Purification of recombinant human and Drosophila septin hexamers for TIRF assays of actin-septin filament assembly. *Methods Cell Biol.* **136**, 199-220. doi:10.1016/bs.mcb.2016.03.020
- McIlhatton, M. A., Burrows, J. F., Donaghy, P. G., Chanduloy, S., Johnston, P. G. and Russell, S. E. (2001). Genomic organization, complex splicing pattern and expression of a human septin gene on chromosome 17q25.3. *Oncogene* **20**, 5930-5939. doi:10.1038/sj.onc.1204752
- McMurray, M. A., Bertin, A., Garcia, G., III, Lam, L., Nogales, E. and Thorner, J. (2011). Septin filament formation is essential in budding yeast. *Dev. Cell* **20**, 540-549. doi:10.1016/j.devcel.2011.02.004
- Mendonca, D. C., Macedo, J. N., Guimaraes, S. L., Barroso da Silva, F. L., Cassago, A., Garratt, R. C., Portugal, R. V. and Araujo, A. P. U. (2019). A revised order of subunits in mammalian septin complexes. *Cytoskeleton (Hoboken)* **76**, 457-466. doi:10.1002/cm.21569
- Momany, M., Pan, F. and Malmberg, R. L. (2008). Evolution and conserved domains of the septins. In *The Septins* (ed. P. A. Hall, S.E.H. Russell and J.R. Pringle), pp. 35-45. John Wiley & Sons, Ltd.
- Montagna, C., Bejerano-Sagie, M. and Zechmeister, J. R. (2015). Mammalian septins in health and disease. *Res. Reports Biochem.* **5**, 59-72. doi:10.2147/RRBC.S59060
- Mostowy, S. and Cossart, P. (2012). Septins: the fourth component of the cytoskeleton. *Nat. Rev. Mol. Cell Biol.* **13**, 183-194. doi:10.1038/nrm3284
- Nagata, K., Kawajiri, A., Matsui, S., Takagishi, M., Shiromizu, T., Saitoh, N., Izawa, I., Kiyono, T., Itoh, T. J., Hotani, H. et al. (2003). Filament formation of MSF-A, a mammalian septin, in human mammary epithelial cells depends on interactions with microtubules. *J. Biol. Chem.* **278**, 18538-18543. doi:10.1074/jbc.M205246200
- Nagata, K., Asano, T., Nozawa, Y. and Inagaki, M. (2004). Biochemical and cell biological analyses of a mammalian septin complex, Sept7/9b/11. *J. Biol. Chem.* **279**, 55895-55904. doi:10.1074/jbc.M406153200
- Nakos, K., Rosenberg, M. and Spiliotis, E. T. (2019). Regulation of microtubule plus end dynamics by septin 9. *Cytoskeleton (Hoboken)* **76**, 83-91. doi:10.1002/cm.21488
- Nishihama, R., Onishi, M. and Pringle, J. R. (2011). New insights into the phylogenetic distribution and evolutionary origins of the septins. *Biol. Chem.* **392**, 681-687. doi:10.1515/BC.2011.086
- Omrane, M., Camara, A. S., Tavenau, C., Benzoubir, N., Tubiana, T., Yu, J., Guerois, R., Samuel, D., Goud, B., Pous, C. et al. (2019). Septin 9 has two polybasic domains critical to septin filament assembly and golgi integrity. *iScience* **13**, 138-153. doi:10.1016/j.isci.2019.02.015
- Ong, K., Wloka, C., Okada, S., Svitkina, T. and Bi, E. (2014). Architecture and dynamic remodelling of the septin cytoskeleton during the cell cycle. *Nat. Commun.* **5**, 5698. doi:10.1038/ncomms5698
- Pan, F., Malmberg, R. L. and Momany, M. (2007). Analysis of septins across kingdoms reveals orthology and new motifs. *BMC Evol. Biol.* **7**, 103. doi:10.1186/1471-2148-7-103
- Pedelacq, J. D., Cabantous, S., Tran, T., Terwilliger, T. C. and Waldo, G. S. (2006). Engineering and characterization of a superfolder green fluorescent protein. *Nat. Biotechnol.* **24**, 79-88. doi:10.1038/nbt1172
- Ribet, D., Boscaini, S., Cauvin, C., Siguier, M., Mostowy, S., Echard, A. and Cossart, P. (2017). SUMOylation of human septins is critical for septin filament bundling and cytokinesis. *J. Cell Biol.* **216**, 4041-4052. doi:10.1083/jcb.201703096
- Rodal, A. A., Kozubowski, L., Goode, B. L., Drubin, D. G. and Hartwig, J. H. (2005). Actin and septin ultrastructures at the budding yeast cell cortex. *Mol. Biol. Cell* **16**, 372-384. doi:10.1091/mbc.e04-08-0734
- Rosa, H. V. D., Leonardo, D. A., Brognara, G., Brandao-Neto, J., D'Muniz Pereira, H., Araujo, A. P. U. and Garratt, R. C. (2020). Molecular recognition at septin interfaces: the switches hold the key. *J. Mol. Biol.* **432**, 5784-5801. doi:10.1016/j.jmb.2020.09.001
- Sala, F. A., Valadares, N. F., Macedo, J. N., Borges, J. C. and Garratt, R. C. (2016). Heterotypic coiled-coil formation is essential for the correct assembly of the septin heterofilament. *Biophys. J.* **111**, 2608-2619. doi:10.1016/j.bpj.2016.10.032
- Schuck, P. and Rossmanith, P. (2000). Determination of the sedimentation coefficient distribution by least-squares boundary modeling. *Biopolymers* **54**, 328-341. doi:10.1002/1097-0282(20001015)54:5<328::AID-BIP40>3.0.CO;2-P
- Sellin, M. E., Sandblad, L., Stenmark, S. and Gullberg, M. (2011). Deciphering the rules governing assembly order of mammalian septin complexes. *Mol. Biol. Cell* **22**, 3152-3164. doi:10.1091/mbc.e11-03-0253
- Sellin, M. E., Stenmark, S. and Gullberg, M. (2014). Cell type-specific expression of SEPT3-homology subgroup members controls the subunit number of heteromeric septin complexes. *Mol. Biol. Cell* **25**, 1594-1607. doi:10.1091/mbc.e13-09-0553
- Shevchenko, A., Tomas, H., Havlis, J., Olsen, J. V. and Mann, M. (2006). In-gel digestion for mass spectrometric characterization of proteins and proteomes. *Nat. Protoc.* **1**, 2856-2860. doi:10.1038/nprot.2006.468
- Shi, X., Lim, J. and Ha, T. (2010). Acidification of the oxygen scavenging system in single-molecule fluorescence studies: in situ sensing with a ratiometric dual-emission probe. *Anal. Chem.* **82**, 6132-6138. doi:10.1021/ac1008749
- Silva, J. C., Gorenstein, M. V., Li, G. Z., Vissers, J. P. and Geromanos, S. J. (2006). Absolute quantification of proteins by LCMSE: a virtue of parallel MS acquisition. *Mol. Cell. Proteomics* **5**, 144-156. doi:10.1074/mcp.M500230-MCP200
- Sirajuddin, M., Farkasovsky, M., Hauer, F., Kuhlmann, D., Macara, I. G., Weyand, M., Stark, H. and Wittinghofer, A. (2007). Structural insight into filament formation by mammalian septins. *Nature* **449**, 311-315. doi:10.1038/nature06052
- Smith, C., Dolat, L., Angelis, D., Forgacs, E., Spiliotis, E. T. and Galkin, V. E. (2015). Septin 9 exhibits polymorphic binding to F-Actin and inhibits myosin and cofilin activity. *J. Mol. Biol.* **427**, 3273-3284. doi:10.1016/j.jmb.2015.07.026
- Soroosh, F., Kim, M. S., Palander, O., Balachandran, Y., Collins, R. F., Benlekhir, S., Rubinstein, J. L. and Trimble, W. S. (2021). Revised subunit order of mammalian septin complexes explains their in vitro polymerization properties. *Mol. Biol. Cell* **32**, 289-300. doi:10.1091/mbc.E20-06-0398
- Spiliotis, E. T., Kinoshita, M. and Nelson, W. J. (2005). A mitotic septin scaffold required for Mammalian chromosome congression and segregation. *Science* **307**, 1781-1785. doi:10.1126/science.1106823
- Spiliotis, E. T., Hunt, S. J., Hu, Q., Kinoshita, M. and Nelson, W. J. (2008). Epithelial polarity requires septin coupling of vesicle transport to polyglutamylated microtubules. *J. Cell Biol.* **180**, 295-303. doi:10.1083/jcb.200710039
- Steinegger, M., Meier, M., Mirdita, M., Vohringer, H., Haunsberger, S. J. and Soding, J. (2019). HH-suite3 for fast remote homology detection and deep protein annotation. *BMC Bioinformatics* **20**, 473. doi:10.1186/s12859-019-0319-7
- Studer, G., Rempfer, C., Waterhouse, A. M., Gummienny, R., Haas, J. and Schwede, T. (2020). QMEANDisCo-distance constraints applied on model quality estimation. *Bioinformatics* **36**, 2647. doi:10.1093/bioinformatics/btaa058

- Surka, M. C., Tsang, C. W. and Trimble, W. S. (2002). The mammalian septin MSF localizes with microtubules and is required for completion of cytokinesis. *Mol. Biol. Cell* **13**, 3532-3545. doi:10.1091/mbc.e02-01-0042
- Szuba, A., Bano, F., Castro-Linares, G., Iv, F., Mavrikakis, M., Richter, R. P., Bertin, A. and Koenderink, G. H. (2021). Membrane binding controls ordered self-assembly of animal septins. *Elife* **10**, e63349. doi:10.7554/eLife.63349
- Tanaka-Takiguchi, Y., Kinoshita, M. and Takiguchi, K. (2009). Septin-mediated uniform bracing of phospholipid membranes. *Curr. Biol.* **19**, 140-145. doi:10.1016/j.cub.2008.12.030
- Taveneau, C., Blanc, R., Pehau-Arnaudet, G., Di Cicco, A. and Bertin, A. (2020). Synergistic role of nucleotides and lipids for the self-assembly of Shs1 septin oligomers. *Biochem. J.* **477**, 2697-2714. doi:10.1042/BCJ20200199
- Taylor, I. A., Rittinger, K. and Eccleston, J. F. (2015). Sedimentation equilibrium studies. In *Methods in Molecular Biology*, Vol. 1278 (ed. C. L. Meyerkord and H. Fu), pp. 205-222. Springer.
- Valadares, N. F., d' Muniz Pereira, H., Ulian Araujo, A. P. and Garratt, R. C. (2017). Septin structure and filament assembly. *Biophys Rev.* **9**, 481-500. doi:10.1007/s12551-017-0320-4
- Verdier-Pinard, P., Salaun, D., Bouguenina, H., Shimada, S., Pophillat, M., Audebert, S., Agavnian, E., Coslet, S., Charafe-Jauffret, E., Tachibana, T. et al. (2017). Septin 9_i2 is downregulated in tumors, impairs cancer cell migration and alters subnuclear actin filaments. *Sci. Rep.* **7**, 44976. doi:10.1038/srep44976
- Versele, M. and Thorner, J. (2004). Septin collar formation in budding yeast requires GTP binding and direct phosphorylation by the PAK, Cla4. *J. Cell Biol.* **164**, 701-715. doi:10.1083/jcb.200312070
- Waterhouse, A., Bertoni, M., Bienert, S., Studer, G., Tauriello, G., Gumienny, R., Heer, F. T., de Beer, T. A. P., Rempfer, C., Bordoli, L. et al. (2018). SWISS-MODEL: homology modelling of protein structures and complexes. *Nucleic Acids Res.* **46**, W296-W303. doi:10.1093/nar/gky427
- Weems, A. and McMurray, M. (2017). The step-wise pathway of septin hetero-octamer assembly in budding yeast. *Elife* **6**, e23689. doi:10.7554/eLife.23689
- Weirich, C. S., Erzberger, J. P. and Barral, Y. (2008). The septin family of GTPases: architecture and dynamics. *Nat. Rev. Mol. Cell Biol.* **9**, 478-489. doi:10.1038/nrm2407
- Winkelman, J. D., Suarez, C., Hocky, G. M., Harker, A. J., Morganthaler, A. N., Christensen, J. R., Voth, G. A., Bartles, J. R. and Kovar, D. R. (2016). Fascin- and alpha-actinin-bundled networks contain intrinsic structural features that drive protein sorting. *Curr. Biol.* **26**, 2697-2706. doi:10.1016/j.cub.2016.07.080
- Xie, H., Surka, M., Howard, J. and Trimble, W. S. (1999). Characterization of the mammalian septin H5: distinct patterns of cytoskeletal and membrane association from other septin proteins. *Cell Motil. Cytoskelet.* **43**, 52-62. doi:10.1002/(SICI)1097-0169(1999)43:1<52::AID-CM6>3.0.CO;2-5
- Xu, J. B. (2019). Distance-based protein folding powered by deep learning. *Proc. Natl. Acad. Sci. USA* **116**, 16856-16865. doi:10.1073/pnas.1821309116
- Zacharias, D. A., Violin, J. D., Newton, A. C. and Tsien, R. Y. (2002). Partitioning of lipid-modified monomeric GFPs into membrane microdomains of live cells. *Science* **296**, 913-916. doi:10.1126/science.1068539
- Zhang, J., Kong, C., Xie, H., McPherson, P. S., Grinstein, S. and Trimble, W. S. (1999). Phosphatidylinositol polyphosphate binding to the mammalian septin H5 is modulated by GTP. *Curr. Biol.* **9**, 1458-1467. doi:10.1016/S0960-9822(00)80115-3
- Zimmermann, L., Stephens, A., Nam, S. Z., Rau, D., Kubler, J., Lozajic, M., Gabler, F., Soding, J., Lupas, A. N. and Alva, V. (2018). A completely reimplemented MPI bioinformatics toolkit with a new HHpred server at its core. *J. Mol. Biol.* **430**, 2237-2243. doi:10.1016/j.jmb.2017.12.007

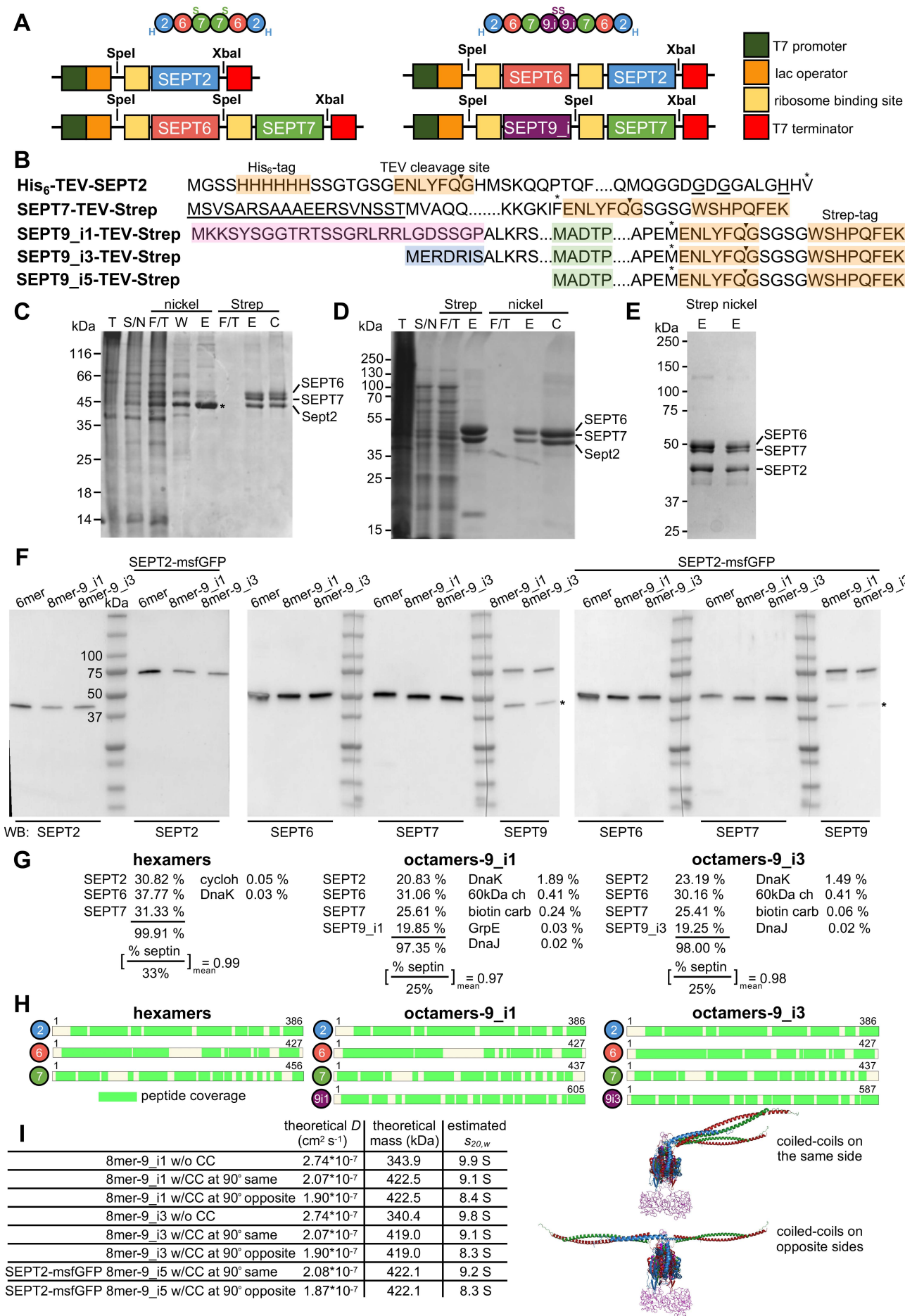


Fig. S1. Isolation and characterization of recombinant human septin octamers containing distinct SEPT9 isoforms. (A) Schematic of the two sets of plasmids used for the co-expression of septins for isolating recombinant human SEPT2-, SEPT6-, SEPT7-containing hexamers (left) and recombinant human SEPT2-, SEPT6-, SEPT7-, SEPT9_i-containing octamers (right) from bacteria. *SpeI* and *XbaI* restriction sites used for subcloning are indicated (see Materials and methods for details). The end subunit (SEPT2) contains an N-terminal TEV-cleavable His₆-tag (depicted as H in the cartoons of the septin complexes), while the central subunit (SEPT7 in hexamers, or SEPT9_i in octamers) contains a C-terminal TEV-cleavable Strep-tag II. The plasmids for the production of fluorescent septin complexes used in this study differ only in that the gene coding for SEPT2 has been replaced by the one encoding SEPT2-msfGFP. **(B)** Primary sequences of the N- and C-termini of tagged septins used in the purification schemes in this study. His₆-tag, Strep-tag-II, and TEV cleavage site sequences are highlighted in light orange. Black arrowheads indicate the position of the TEV cleavage site. Asterisks point to the last amino acid of the respective septin sequence. The underlined amino acids in the C-terminus of SEPT2 are three out of the five residues that differ among the mouse and human homologs. The underlined stretch of N-terminal residues in SEPT7 was missing in previously reported plasmids (see Materials and methods for details). SEPT9 long isoform-specific sequences are highlighted in pink and cyan (see Fig. 1B). The sequence depicting the onset of the short isoform SEPT9_i5, which is also contained in the N-terminal extensions of the long isoforms, is highlighted in green. **(C-E)** SDS-PAGE analysis of the purification of mammalian (C and D) and human (E) SEPT2-, SEPT6-, SEPT7-containing hexamers. Coomassie-stained gels show fractions from the total lysate (T), supernatant (S/N), flow-through (F/T), wash (W), eluate (E), and after concentration (C), using a two-tag purification scheme employing either a nickel affinity step followed by a Strep-Tactin affinity step (C), or a Strep-Tactin affinity step followed by a nickel affinity step (D and E). Molecular weight markers are shown on the left of each gel. The identification of bands is based on mass spectrometry analysis. The asterisk in (C) points to putative His₆-tagged SEPT2 homodimers that are removed in the Strep-tag affinity step. **(F)** Purified recombinant nonfluorescent and fluorescent (SEPT2-msfGFP) 6mer, 8mer-9_i1 and 8mer-9_i3 were analyzed by SDS-PAGE, followed by Western blot (WB) with antibodies against SEPT2, SEPT6, SEPT7, and SEPT9, as indicated at the bottom of each gel (see Materials and methods for details). Molecular weight markers are shown for the first gel; the same markers were used in all gels. All septins were intact, the long N-terminal extension of SEPT9 being most sensitive to proteolysis (the asterisk points to a degradation product for SEPT9). See Materials and methods for the theoretical and apparent molecular masses. **(G-H)** Examples of mass spectrometry analysis of recombinant 6mer, 8mer-9_i1 and 8mer-9_i3 preps. Calculations of the mol fractions of septins and contaminants in the respective protein preps are shown (G) using the Top3 quantitation approach (see Materials and methods for details). The obtained mol fractions of septins, compared with the theoretical ones in 6mer (33%) and 8mer (25%), point to the isolation of stoichiometric 6mers and 8mers. Examples of tryptic peptide coverage for individual septins in recombinant 6mer, 8mer-9_i1 and 8mer-9_i3 preps (H), supporting that the isolated septin complexes are intact. **(I)** Models for octamers without coiled-coils, or with coiled-coils at 90° with respect to the α_6 helix, pointing to the same or to opposite directions as shown on the right for a model of an octamer-9_i1, were used to calculate their theoretical sedimentation coefficients (see Materials and methods for details). The N-terminal extensions of SEPT9_i1, SEPT9_i3 and SEPT9_i5 were modeled as random coils in the models used in these calculations. The absence of coiled-coils altogether is predicted to make the complexes sediment faster by ~ 0.8 S. Coiled-coils lying on the same side tend to make complexes more compact and thus slightly accelerate sedimentation by ~ 0.1-0.5 S, whereas coiled-coils on opposite sides are predicted to slow down sedimentation by ~ 0.6-0.7 S units.

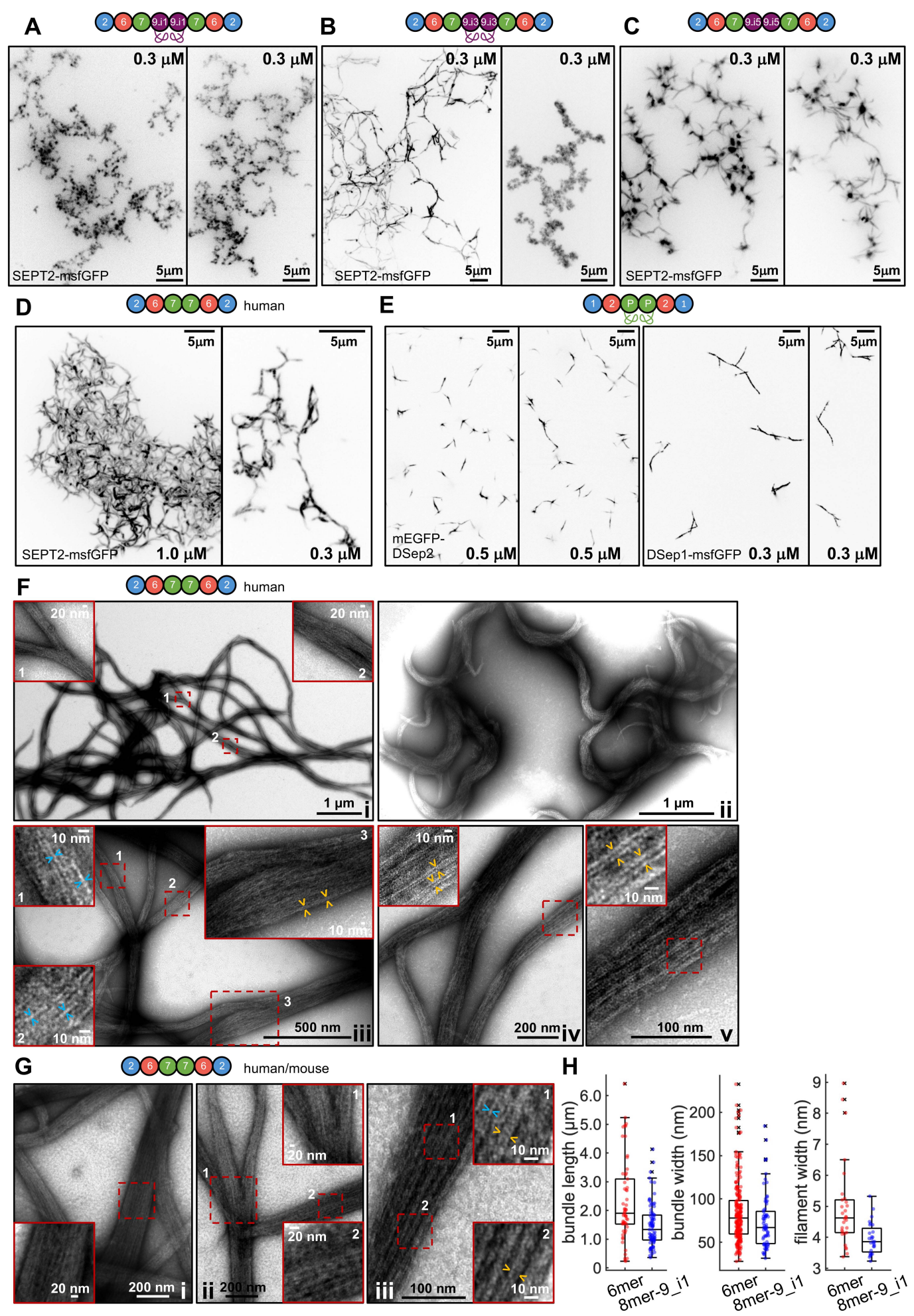


Fig. S2. *In vitro* reconstitution of septin polymerization in solution using recombinant animal septin hexamers and octamers. (A-C) Representative spinning disk fluorescence images of higher-order filament assemblies upon polymerization of human 8mer-9_i1 (A), 8mer-9_i3 (B) and 8mer-9_i5 (C) after dilution into low salt conditions (50 mM KCl) at the indicated final octamer concentration. Two examples are shown for each. All images shown are maximum-intensity projections and use an inverted grayscale. (D-E) Representative spinning disk fluorescence images of higher-order filament assemblies upon polymerization of human SEPT2-, SEPT6-, SEPT7-containing hexamers (D) and *Drosophila* DSep1-, DSep2-, Peanut-containing hexamers (E) after dilution into low salt conditions (50 mM KCl) at the indicated final concentration. Two different *Drosophila* hexamers are shown: hexamers labeled with mEGFP-DSep2 (left panel in E) and hexamers labeled with DSep1-msfGFP (right panel in E). Two examples are shown for each type of hexamer. *Drosophila* hexamers organize in straight needle-like bundles, in line with previous reports (Mavrakakis et al., 2014; Mavrakakis et al., 2016). The freehand line preceding the G domain of Peanut in the hexamer cartoon above the images depicts its large N-terminal extension. Images in (D) are maximum-intensity projections. All images shown use an inverted grayscale. (F) Negative-stain EM images of higher-order filament assemblies upon polymerization of human 6mer at 0.2 μ M and at low salt (50 mM KCl). The insets show magnifications of selected regions of interest (dashed rectangles in red), and highlight single septin filaments (blue arrowheads), paired septin filaments (orange arrowheads), and splayed filament bundles (i, iii). (G) Negative-stain EM of higher-order filament assemblies upon polymerization of mouse SEPT2-, human SEPT6-, human SEPT7 Δ N19-containing hexamers at low salt (50 mM KCl) and at 1 μ M (i, ii) or 0.5 μ M (iii). The insets show magnifications of selected regions of interest (dashed rectangles in red), and highlight single septin filaments (blue arrowheads), paired septin filaments (orange arrowheads), and splayed filament bundles (ii). (H) Box plots showing the distribution of septin filament bundle lengths (left), septin filament bundle widths (middle) and septin filament widths within bundles (right), measured from electron micrographs, and comparing human 6mer- (red-filled circles) and 8mer-9_i1 (blue-filled circles) filament assemblies. The data points are plotted on top of the respective box plots. On each box, the central mark indicates the median, and the bottom and top edges of the box indicate the 25th and 75th percentiles, respectively. The whiskers extend to the most extreme data points not considered outliers, and the outliers are plotted individually using the 'x' symbol. The number of measurements in each box plot, ordered from left to right, is $n = 58, 83, 229, 69, 30, 28$. The respective median values are 1.9 μ m, 1.3 μ m, 78 nm, 67 nm, 4.6 nm, and 3.9 nm.

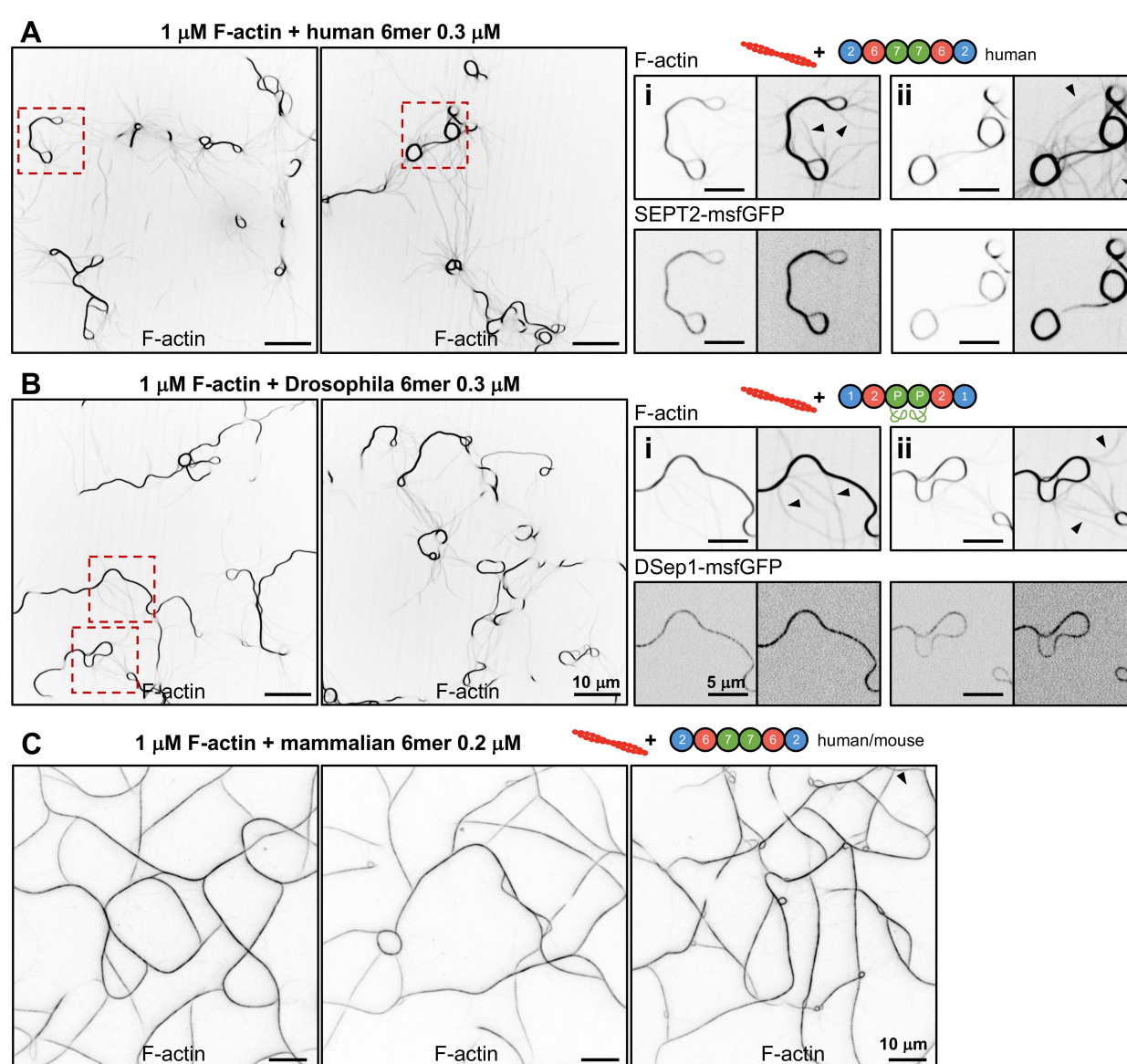


Fig. S3. *In vitro* reconstitution of actin filament cross-linking by recombinant animal septin hexamers. (A-C) Representative spinning disk fluorescence images of reconstituted actin filaments, polymerizing in the presence of human SEPT2-, SEPT6-, SEPT7-containing hexamers (A), *Drosophila* DSep1-, DSep2-, Peanut-containing hexamers (B), and mouse SEPT2-, human SEPT6-, human SEPT7 Δ N19-containing hexamers (C), prepared as in Fig.4C-D. (A-B) Actin filaments are visualized with AlexaFluor568-conjugated phalloidin, and septins with SEPT2-msfGFP (human) or DSep1-msfGFP (*Drosophila*). Two examples of large fields of view are shown for each, depicting the similar cross-linking of actin filaments into actin filament bundles in the presence of both types of hexamers; only actin labeling is shown. Insets on the right side of each panel show higher magnifications of selected regions of interest on the left (dashed squares in red). Two regions of interest (i, ii) are shown in each case, depicting both the actin (top row) and septin (bottom row) signals. For each inset, actin and septin signals are shown in duplicates: the first set shows the raw signals without any saturation, whereas the second set, adjacent to the first one, shows both actin and septin signals after deliberate contrast enhancement. The contrast-enhanced images in the actin channel saturate the actin bundles, while bringing out weaker-intensity single actin filaments (black arrowheads). The respective contrast-enhanced images in the septin channel show the presence of septins in actin bundles, but their absence from single actin filaments. Scale bars in all large fields of views, 10 μ m. Scale bars in all insets, 5 μ m. (C) Actin filaments are visualized with Alexa Fluor 488-G-actin and septins are nonfluorescent. Three examples of large fields of view are shown, depicting the similar cross-linking of actin filaments into actin filament bundles. Scale bars in all large fields of views, 10 μ m. All images shown use an inverted grayscale.

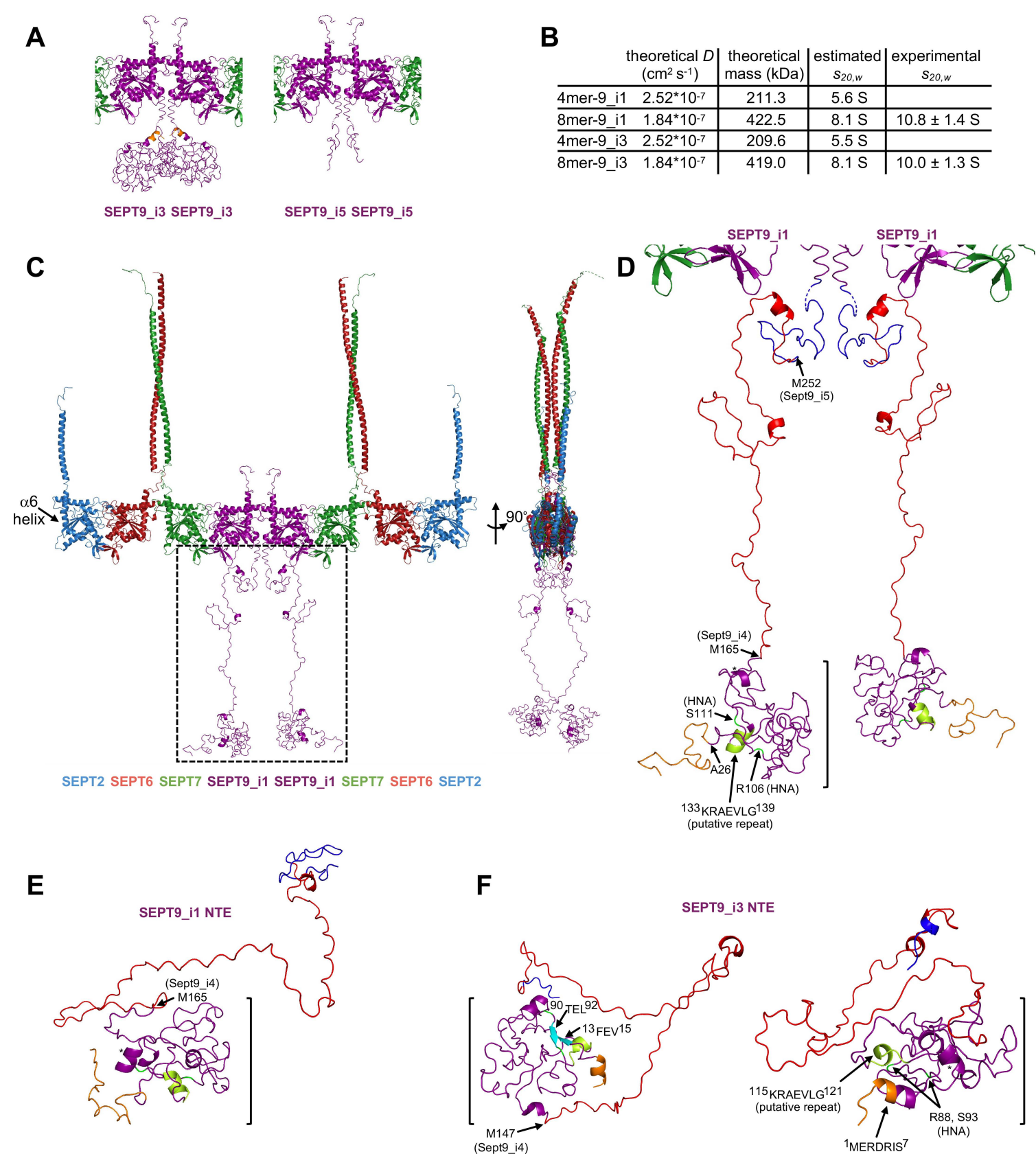


Fig. S4. Modeling of the N-terminal extensions of SEPT9_i1, SEPT9_i3 and SEPT9_i5. (A) Models of the N-terminal extensions of SEPT9_i3 (left) and SEPT9_i5 (right) as random coils in the context of the respective octamers (only the central SEPT9 dimer is shown for simplicity); compare with Fig. 1H for SEPT9_i1. The N-terminal sequence specific to SEPT9_i3 is depicted in orange. (B-C) Model of a human octamer-9_i1 built as in Fig. 1H, now depicting the N-terminal extension of SEPT9_i1 in an extended conformation as predicted by RaptorX (see Materials and methods for details). An *en face* view (left) and a side view after a 90° rotation (right) are shown. Generated models containing this extended conformation were used to calculate the theoretical sedimentation coefficients for comparison with the experimentally obtained ones (table in C). Such models predict sedimentation coefficients that are much smaller than the experimentally measured ones, suggesting that the N-terminal extensions adopt a more compact/globular conformation in solution and in the absence of any interacting partners. (D) The extended conformation of the N-terminal extension (NTE) of SEPT9_i1 (dashed rectangle in B) is annotated as follows. The N-terminal stretch, in orange, depicts the sequence specific to SEPT9_i1; the remaining of the sequence, starting at Ala26 (A26), is common with the other long SEPT9 isoforms (SEPT9_i2 and SEPT9_i3). Residues Met165 (M165) and Met252 (M252) depict the onset of the short isoforms SEPT9_i4 and SEPT9_i5, respectively. The N-terminus of SEPT9_i4 until the onset of the region shared with SEPT9_i5 is shown in red; the N-terminus of SEPT9_i5 until the onset of the α 0 helix is shown in blue. Residues Arg106 (R106) and Ser111 (S111), in green, are mutated in HNA. The helix comprising residues KRAEVLG, colored in lime, depicts a putative imperfect repeat identified in Verdier-Pinard et al., 2017. (E-F) Alternative models for the NTE of SEPT9_i1 (E) and the NTE of SEPT9_i3 (F) as predicted by RaptorX. The N-terminal sequence specific to SEPT9_i3 is depicted in orange; both Phyre2 (A) and RaptorX (F) model this sequence as a helix. The color code of the annotated residues is the same as for (D). The β -strands in cyan in the left model in (F) depict short β -strands predicted previously in Verdier-Pinard et al., 2017. The asterisks in D-F point to the sequence SKQVEN modeled as a helix. All models shown in D-F are hypothetical; potentially disordered NTEs of SEPT9 could conceivably become structured in the presence of interacting surfaces, for example, cell membranes, and binding partners. Interestingly, the predicted contact probability matrices of both SEPT9_i1 and SEPT9_i3 suggest that the first half of their N-terminal extension, which is unique to the long SEPT9 isoforms, forms potentially a structured domain (brackets in D-F), whereas the second half, which corresponds to the sequence shared with the short isoforms SEPT9_i4 and SEPT9_i5, is largely disordered.

Table S1. Extinction coefficients and molecular masses used for concentration conversions for recombinant human septin complexes purified in this study.

	MW (kDa)	$\epsilon_{280\text{nm}}$ $\text{L.g}^{-1}.\text{cm}^{-1}$	
human hexamers	291.8	0.563	1 g/L= 3.4 μM
human octamers-9_i1	422.5	0.505	1 g/L= 2.4 μM
human octamers-9_i3	419.0	0.502	1 g/L= 2.4 μM
human octamers-9_i5	368.7	0.570	1 g/L= 2.7 μM
SEPT2-msfGFP human hexamers	345.2	0.586	1 g/L= 2.9 μM
SEPT2-msfGFP human octamers-9_i1	475.9	0.527	1 g/L= 2.1 μM
SEPT2-msfGFP human octamers-9_i3	472.4	0.525	1 g/L= 2.1 μM
SEPT2-msfGFP human octamers-9_i5	422.1	0.588	1 g/L= 2.4 μM



Movie 1. Polymerization of recombinant human septin octamers-9_i3. Optical sectioning (z-stack with a Δz interval of 0.5 μm) in the bulk of a flow channel depicting SEPT2-msfGFP human septin octamer-9_i3 polymerized at 0.3 μM (100% GFP-septins) by dilution into low-salt (50 mM KCl) buffer. Spinning disk fluorescence images displayed at 5 frames per second. Related to Fig. S2 B.



Movie 2. Reconstitution of single actin filaments. Time-lapse sequence (Δt interval of 0.5 s) at the surface of a PLL-PEG passivated glass coverslip showing single fluctuating actin filaments at 1 μM . G-actin was polymerized in the presence of Alexa Fluor 568-phalloidin. Spinning disk fluorescence images displayed at 5 frames per second. A still image from this time lapse sequence is shown in Fig. 4A.



Movie 3. Actin filament cross-linking by recombinant human septin octamers-9_i1. Time-lapse sequence (Δt interval of 0.5 s) at the surface of a PLL-PEG passivated glass coverslip showing cross-linked actin filaments (at 1 μM) in the presence of SEPT2-msfGFP human septin octamer-9_i1 at 0.3 μM (20% GFP-septins). G-actin was polymerized in the presence of Alexa Fluor 568-phalloidin. The actin channel is shown. Spinning disk fluorescence images, using an inverted grayscale, are displayed at 5 frames per second. A still image from this time lapse sequence is shown in Fig. 4C.